



Contents lists available at ScienceDirect

## Journal of Neuroscience Methods

journal homepage: [www.elsevier.com/locate/jneumeth](http://www.elsevier.com/locate/jneumeth)

## An MRI protocol for anatomical and functional evaluation of the California sea lion brain

Peter F. Cook<sup>a</sup>, Vanessa A. Hoard<sup>b</sup>, Sudipto Dolui<sup>c</sup>, Blaise deB Frederick<sup>d,e</sup>, Richard Redfern<sup>f</sup>, Sophie E. Dennison<sup>g</sup>, Barbie Halaska<sup>b</sup>, Josh Bloom<sup>h</sup>, Kris T. Kruse-Elliott<sup>h</sup>, Emily R. Whitmer<sup>b</sup>, Emily J. Trumbull<sup>b</sup>, Gregory S. Berns<sup>i</sup>, John A. Detre<sup>c,j</sup>, Mark D'Esposito<sup>f,k</sup>, Frances M. D. Gulland<sup>l</sup>, Colleen Reichmuth<sup>m</sup>, Shawn P. Johnson<sup>b</sup>, Cara L. Field<sup>b</sup>, Ben A. Inglis<sup>f,\*</sup>

<sup>a</sup> Department of Biopsychology, New College of Florida, 5800 Bay Shore Road, Sarasota, FL, 34243, USA

<sup>b</sup> The Marine Mammal Center, 2000 Bunker Road, Sausalito, CA, 94965, USA

<sup>c</sup> Department of Radiology, University of Pennsylvania Perelman School of Medicine, 3400 Spruce Street, Philadelphia, PA, 19104, USA

<sup>d</sup> Department of Psychiatry, Harvard University Medical School, 25 Shattuck St, Boston, MA, 02115, USA

<sup>e</sup> McLean Hospital Brain Imaging Center, 115 Mill St., Belmont, MA, 02478, USA

<sup>f</sup> Henry H. Wheeler, Jr. Brain Imaging Center, 188 Li Ka Shing Center for Biomedical and Health Sciences, University of California, Berkeley, CA, 94720, USA

<sup>g</sup> TeleVet Imaging Solutions, PLLC, Oakton, VA, 22124, USA

<sup>h</sup> AnimalScan Advanced Veterinary Imaging, 934 Charter St, Redwood City, CA, 94063, USA

<sup>i</sup> Psychology Department, Emory University, 36 Eagle Row, Atlanta, GA, 30322, USA

<sup>j</sup> Department of Neurology, University of Pennsylvania, 3400 Spruce St, Philadelphia, PA, 19104, USA

<sup>k</sup> Helen Wills Neuroscience Institute, University of California, 132 Barker Hall, Berkeley, CA, 94720, USA

<sup>l</sup> School of Veterinary Medicine Wildlife Health Center, University of California at Davis, 1089 Veterinary Medicine Dr, Davis, CA, 95616, USA

<sup>m</sup> Long Marine Laboratory, Institute of Marine Sciences, University of California at Santa Cruz, 115 McAllister Way, Santa Cruz, CA, 95060, USA

## ARTICLE INFO

## Keywords:

California sea lion  
Pinniped  
Domoic acid  
Epilepsy  
Hippocampus  
MRI

## ABSTRACT

**Background:** Domoic acid (DOM) is a neurotoxin produced by some harmful algae blooms in coastal waters. California sea lions (*Zalophus californianus*) exposed to DOM often strand on beaches where they exhibit a variety of symptoms, including seizures. These animals typically show hippocampal atrophy on MRI scans.

**New Method:** We describe an MRI protocol for comprehensive evaluation of DOM toxicosis in the sea lion brain. We intend to study brain development in pups exposed *in utero*. The protocol depicts the hippocampal formation as the primary region of interest. We include scans for quantitative morphometry, functional and structural connectivity, and a cerebral blood flow map.

**Results:** High-resolution 3D anatomical scans facilitate *post hoc* slicing in arbitrary planes and accurate morphometry. We demonstrate the first cerebral blood flow map using MRI, and the first structural tractography from a live sea lion brain.

**Comparison with Existing Methods:** Scans were compared to prior anatomical and functional studies in live sea lions, and structural connectivity in post mortem specimens. Hippocampal volumes were broadly in line with prior studies, with differences likely attributable to the 3D approach used here. Functional connectivity of the dorsal left hippocampus matched that found in a prior study conducted at a lower magnetic field, while structural connectivity in the live brain agreed with findings observed in post mortem studies.

**Abbreviations:** A-P, anterior-to-posterior; ACR, American College of Radiology; ACVR, American College of Veterinary Radiology; ASL, arterial spin labeling; ATT, arterial transit time; BIC, Brain Imaging Center; CBF, cerebral blood flow; CSF, cerebrospinal fluid; dMRI, diffusion magnetic resonance imaging; DOM, domoic acid; DTI, diffusion tensor imaging; EPI, echoplanar imaging; FA, fractional anisotropy; FLAIR, fluid-attenuated inversion recovery; fMRI, functional magnetic resonance imaging; GM, gray matter; GRAPPA, generalized autocalibrating partially parallel acquisitions; HAB, harmful algae bloom; H-F, head-to-foot; L-R, left-to-right; MIP, maximum intensity projection; MPRAGE, magnetization-prepared rapid acquisition of gradient echo; mTLE, mesial temporal lobe epilepsy; PCASL, pseudo-continuous arterial spin labeling; PLD, post labeling delay; PWI, perfusion-weighted image; rCBF, regional cerebral blood flow; RF, radiofrequency; R-L, right-to-left; SFDK, Six Flags Discovery Kingdom; SMS, simultaneous multislice; SPACE, Sampling Perfection with Application optimized Contrasts by using different flip angle Evolutions; T<sub>1</sub>, longitudinal relaxation time; T<sub>2</sub>, transverse relaxation time; TE, echo time; TMMC, The Marine Mammal Center; TOF, time-of-flight; TR, repetition time; WM, white matter.

\* Corresponding author.

E-mail address: [binglis@berkeley.edu](mailto:binglis@berkeley.edu) (B.A. Inglis).

<https://doi.org/10.1016/j.jneumeth.2021.109097>

Received 13 October 2020; Received in revised form 29 January 2021; Accepted 4 February 2021

Available online 10 February 2021

0165-0270/© 2021 Elsevier B.V. All rights reserved.

**Conclusions:** Our protocol provides a comprehensive, longitudinal view of the functional and anatomical changes expected to result from DOM toxicosis. It can also screen for other common neurological pathologies and is suitable for any pinniped that can fit inside an MRI scanner.

## 1. Introduction

Harmful algae blooms (HABs) are a worldwide oceanic phenomenon that present a variety of hazards for marine wildlife depending on the algae species and the conditions giving rise to algae growth. Phytoplankton blooms of diatoms in the genus *Pseudo-nitzschia* are a major concern for marine mammals because they can produce the potent excitatory neurotoxin domoic acid (DOM) (Bates et al., 2018). While apparently non-toxic to fish species at naturally occurring levels (Lefebvre et al., 2012), DOM enters the food web by accumulating in the viscera of filter-feeding finfish and shellfish such as anchovies, sardines, crabs, clams, mussels and oysters (Bejarano et al., 2008). Consumption by marine mammals of fish containing DOM can lead to mass mortality and stranding events. Stranded animals can exhibit a variety of symptoms depending on the duration and level of DOM exposure. Acute exposure to high levels can be fatal (Scholin et al. 2000). Animals exposed chronically to lower levels may strand exhibiting symptoms consistent with brain damage, including epilepsy (Goldstein et al., 2008). The severity and extent of DOM-producing HABs are increasing worldwide, leading to increased potential for both marine mammal and human exposure to DOM (McKibben et al., 2017; Wohlrab et al., 2020).

The coastal Pacific Ocean has experienced several large HABs in the past two decades (McCabe et al., 2016; Zhu et al., 2017). California sea lions (*Zalophus californianus*) have thus emerged as a focal species for the study of the effects of naturally-occurring DOM in the environment. Research on rehabilitating sea lions has confirmed that high levels of DOM in pregnant mothers can be transferred (with potentially amplified effects) to their pups *in utero* (Brodie et al., 2006; Costa et al., 2010) and *via* lactation (Rust et al., 2014), raising concerns that maternal exposure could result in devastating health effects expressed much later in development (Lefebvre et al., 2018). We are planning a longitudinal study to identify etiology, symptomatology, and pathology of prenatal exposure to DOM. Here, we describe a detailed MRI protocol for application to sea lions between 6 months and 4 years of age. Our objectives are to provide accurate morphometry of brain structures thought to be at highest risk from DOM toxicosis, to map structural and functional connectivity between the highest risk regions and the rest of the brain, and to define more sensitive and specific clinical criteria for diagnosing DOM toxicosis in wild animals that strand.

Domoic acid toxicosis was first confirmed in California sea lions in 2000 following a mass stranding event in Monterey Bay in 1998 (Scholin et al., 2000). Acute symptoms included seizures, head weaving, scratching and vomiting (Gulland et al., 2002). Chronic exposure to DOM produces an epileptic syndrome in sea lions characterized by behavioral changes, seizures and atrophy of the hippocampal formation (Goldstein et al., 2008; Thomas et al., 2010; Buckmaster et al., 2014). Histology shows hippocampal sclerosis, especially of dentate gyrus and pyramidal cells of CA1, CA3 and CA4, along with gliosis (Scholin et al., 2000; Gulland et al., 2002; Silvagni et al., 2005), and lesions are frequently unilateral (Buckmaster et al., 2014).

Prior MRI scans at 1.5 T revealed considerable abnormal brain anatomy in sea lions exposed to DOM. Of forty-two sea lions with suspected DOM toxicosis, MRI revealed hippocampal atrophy in 41 individuals, accompanied by thinning of the parahippocampal gyrus in 28 individuals, increases in ventricle (temporal horn) size in 34 individuals, and hyperintensity consistent with gliosis in the parahippocampus in 19 individuals (Goldstein et al., 2008). The scan protocol included two-dimensional (2D) proton density-weighted, T<sub>2</sub>-weighted and T<sub>2</sub>-weighted FLAIR (fluid-attenuated inversion recovery) scans, plus a three-dimensional (3D) T<sub>1</sub>-weighted gradient echo scan. Lesions were

best detected in the T<sub>2</sub>-FLAIR scan. We therefore include a 3D T<sub>2</sub>-FLAIR for clinical evaluations in the present protocol, with the 3D format allowing arbitrary plane selections during processing, while scanning with isotropic spatial resolution in three dimensions is better suited to quantitative morphometry.

Detailed anatomical imaging of the California sea lion brain was also performed by Montie et al. (2009, 2010) to establish healthy baselines of living individuals. They found T<sub>2</sub>-weighted images were preferable to T<sub>1</sub>-weighted scans for identifying normal brain structures. We therefore include a T<sub>2</sub>-weighted scan for structure determination and comparison with a prior atlas (Montie et al., 2009).

Recently, Cook et al. (2018) used tractography from diffusion MRI (dMRI) to investigate the effects of DOM on hippocampal connectivity in a small sample of post mortem specimens with and without clinical signs of DOM toxicosis. The DOM brains showed clear evidence of reduced hippocampal volume, and potential signs of white matter (WM) pathology in the fornix, including reduced fractional anisotropy (FA) and increased mean diffusivity (MD). In addition, these brains showed increased WM connectivity between the hippocampus and thalamus. These findings mirror those in humans with mesial temporal lobe epilepsy (mTLE) (Concha et al., 2010; Dinkelacker et al., 2015; Otte et al., 2012), and add support to the idea that wild sea lions with DOM toxicosis might be used as natural models for studying the effects of epilepsy (Buckmaster et al., 2014; Ramsdell and Gulland, 2014). We therefore include dMRI in the protocol, and present here a preliminary report of structural connectivity from a live sea lion brain.

Behaviorally, disruptions in habituation and sensitization, as well as in spatial memory, have been documented in sea lions with hippocampal atrophy associated with DOM toxicosis (Cook et al., 2011, 2015, 2016). In a sample of 27 wild sea lions undergoing rehabilitation, Cook et al. (2016) documented behavioral perseveration in animals with reduced ventral hippocampal volume as measured by MRI. This result was in line with studies showing altered attention and reactivity in rodents with laboratory exposure to DOM (Arkhipov et al., 2008; Zuloaga et al., 2016) and may be related to observations of repetitive behaviors in DOM-exposed sea lions (Goldstein et al., 2008). In another sample of 30 wild sea lions, Cook et al. (2015) found altered performance in a T-maze and a daily foraging task related to reduced dorsal right hippocampal volume, which indicated impaired allocentric memory. The same hippocampal region is involved in allocentric spatial memory in humans (Eichenbaum et al., 2016) and rodents (Moser and Moser, 1998). A subset of 11 sea lions from these two studies also underwent functional MRI (fMRI) at 1.5 T. Evidence of reduced functional connectivity between the hippocampus and thalamus was found in animals with DOM toxicosis and resultant hippocampal atrophy (Cook et al., 2015). We include a similar fMRI scan in the current protocol, seeking to exploit the greater blood oxygenation level-dependent (BOLD) contrast at 3 T than the prior study at 1.5 T.

Epileptic seizures are common in sea lions that strand with likely exposure to DOM (Goldstein et al., 2008). In general, these symptoms are associated with atrophy of the hippocampal formation and are consistent with mTLE. Epileptogenic pathology can be difficult to detect with MRI, and high resolution and contrast are required to delineate the hippocampal formation. Our protocol takes into consideration many of the recommendations of a consensus report on epilepsy in veterinary medicine (Rusbridge et al., 2015) and a suggested protocol for detection of epileptogenic lesions in outpatient human studies (Wellmer et al., 2013).

We also propose to map cerebral blood flow (CBF). Arterial spin labeling (ASL) MRI offers a non-invasive, whole brain measure of CBF

with 2–3 mm spatial resolution. The CBF is usually considered to be tightly coupled with cerebral glucose metabolism (Newberg et al., 2005). Abnormally high regional CBF (rCBF) has been detected in the peri-ictal period of humans with epilepsy (Nguyen et al., 2010; Yoo et al., 2017), including in newborns (Mabray et al., 2018). In the interictal periods, however, epilepsy is often characterized by reduced CBF in the epileptogenic regions (Detre and Alsop, 1999; Wolf et al., 2001). Patients with temporal lobe epilepsy were found to have asymmetric rCBF whether there was evidence of hippocampal sclerosis or not, although the patterns of rCBF abnormalities were different with sclerosis (Guo et al., 2015). However, extant ASL sequences are optimized for the vascular distances, transit delays and geometry of the human brain, and the kinetic models used to compute CBF rely on assumptions that may not hold in other species. Anesthesia further complicates the picture. To address these issues, we have performed empirical tests to determine whether reasonable CBF mapping in pinnipeds is feasible, and we report preliminary evidence to suggest that sea lion vasculature and blood flow dynamics sufficiently resemble those of humans to permit use of human ASL methods.

To summarize, the scan protocol for studying a developing sea lion brain comprises three types of 3D anatomical MRI, functional MRI, a blood perfusion (*i.e.* CBF) mapping scan, and diffusion MRI. Together, these scanning approaches should facilitate a holistic assessment of the neural effects of DOM toxicity. The entire protocol is constrained by the allowable time under anesthesia, for which we use 1-hr as a guideline because it has been well tolerated by sea lions previously, including animals under a year old. Allowing 15-min for intubation, positioning and final health check before the scan commences yields a target maximum protocol duration of 45-min, which must include localizer scans and other scanner adjustments.

## 2. Materials and methods

### 2.1. MRI protocol development

The protocol was developed at the Henry H. Wheeler, Jr. Brain Imaging Center (BIC) at UC Berkeley, on a 3 T Siemens TIM/Trio MRI scanner running version B17A software. Initial tests were performed on post mortem, formalin-fixed sea lion brains provided by The Marine Mammal Center (TMMC), Sausalito CA. A 32-channel receive-only head radiofrequency (RF) coil was used to establish the spatial parameters required to avoid signal aliasing and to fix approximate scan duration limits commensurate with image signal-to-noise ratios (SNR). The pilot protocol was then applied on post mortem brains using a 4-channel human neck RF coil in anticipation of scanning live animals. The neck coil (dimensions: L = 190 mm, W = 330 mm, H = 332 mm) is a ring shape, fully open back and front, that is suitable for intubated live animals. The neck coil was previously used in a study of trained dogs (Berns et al., 2017).

An issue identified during pilot scanning on post mortem specimens was the relatively poor performance of acceleration by under-sampling of k-space when using the 4-channel neck coil. The four loops of the array – two loops in the upper half, two in the lower half - offer limited spatial information for reconstruction methods such as GRAPPA (Griswold et al., 2002) compared to a 12-channel or 32-channel array coil as for human brain imaging. We observed residual aliasing artifacts across the image in the under-sampled dimension. Accordingly, we made the decision to use full k-space sampling without acceleration in most live sea lion scans. An exception was the T<sub>2</sub>-weighted 3D anatomical scan, which would have required a prohibitively long scan duration without acceleration. We also opted not to use simultaneous multi-slice (SMS) acquisition for fMRI or dMRI, again because of the risk of artifacts. Acceleration methods might be included later, if a larger phased-array coil is available to replace the 4-channel neck coil.

### 2.2. Animal procedures

Scanning was performed on five California sea lions undergoing rehabilitation at TMMC. All animals either had symptoms consistent with DOM toxicosis or other abnormal neurological conditions. Scans were also performed on two sea lions housed at Six Flags Discovery Kingdom (SFDK) in Vallejo, CA. The SFDK animals comprised one 3-year-old male adopted from TMMC after repeated strandings and subsequently diagnosed with epilepsy, and one captive-bred 7-month-old pup. The TMMC animals were treated under an authorization granted to the Marine Mammal Health and Stranding Response Program by the National Marine Fisheries Service scientific research permit 18786–04, and approved by the Institutional Animal Care and Use Committee (IACUC) at TMMC. Procedures on the SFDK animals were approved by the animal welfare committee of SFDK. The Office of Laboratory Animal Care at UC Berkeley determined that no formal oversight was required by the Berkeley animal care committee since the scans were clinical evaluations performed as part of the animals' standard veterinary care under the authorization of TMMC or SFDK, and with all medical procedures and welfare monitoring conducted by their veterinary staff. Key data on study animals is included in Table 1.

The MRI suite was prepared for scanning by removing extraneous furniture and impediments to the large number of staff required to transport and monitor an animal under anesthesia. Plastic sheeting was laid on all carpeted floor areas for hygiene. All participants received an MRI safety briefing, and plans and procedures were reviewed by senior personnel at the start of each scan session. During a session, an experienced BIC staff member was assigned as the duty safety officer and was given the sole task of observing activities to identify the development of any potentially hazardous situations. Access to the magnet room – designated Zone IV according to the American College of Radiology (ACR) safety zones principle - was restricted to designated veterinary care staff, all of whom were fully screened for MRI risks. Equipment and supplies required for maintenance of anesthesia and animal monitoring were pre-approved for Zone IV use by BIC staff. All other items were prohibited from Zone IV without the consent of the duty safety officer.

The sea lion transport crate was located outside the scanner suite in a corridor (ACR Zone II) and the anesthesia rig stationed nearby. The lack of an MRI-compatible anesthesia machine and ventilator necessitated patient induction in the corridor, followed by relocation to the operator room (ACR Zone III) for the duration of the MRI scan. Inhalant anesthetic gas (isoflurane in oxygen) delivery to the magnet in Zone IV was through a 10-m rubber hose carrying oxygen and inhalant. The hose was run *via* a waveguide between Zones III and IV. The distance from waveguide to magnet center is comparable to the distance from the waveguide to the corridor, allowing the use of the same hose for anesthesia induction and maintenance, with minimal delay for switching.

Animal handling and anesthesia procedures were established by veterinary staff of TMMC and SFDK in consultation with a veterinary anesthesiologist (KK-E). Animals were fasted overnight to ensure an empty stomach. If necessary, an animal was sedated *via* intramuscular injection of midazolam (0.1–0.3 mg/kg), butorphanol (0.1–0.3 mg/kg) and medetomidine (0.1–0.3 mg/kg) *via* syringe while the animal was still in the transport crate. Once sedated, the crate door was opened and a conical face mask fitted over the muzzle. Anesthesia was induced with 5% isoflurane in oxygen. As soon as jaw tone was absent, the animal was removed from the crate onto a towel or tarpaulin on the floor, then lifted onto the foam pad of an MRI compatible gurney. The foam pad was then lifted onto the gurney at its lowest height for endotracheal intubation. Following intubation, animals were maintained at an appropriate level of isoflurane and, at the lead veterinarian's discretion, the sedative medetomidine was reversed with intramuscular atipamezole (0.1 mg/kg). The MRI compatible gurney was found to be useful for safe and efficient animal handling, including the largest animal scanned so far (96 kg). The gurney's height could then be lifted to its maximum extent with the animal completely supported, obviating the need to lift or



**Table 1**Key data for California sea lion (*Zalophus californianus*) subjects.

Subject identification	Age	Sex	Weight (kg)	Length (cm)	Reason for MRI	HCT	HR at start of MRI	HR at end of MRI	Average RR during MRI
<i>Cronut</i>	~3 years	M	96	190	Epilepsy	0.470	52	51	53.6
<i>Minnow</i>	7 months	M	24.5	115	Healthy control	0.399	106	N/A	N/A
<i>Hammond</i>	~1 year	M	34	122	Multiple seizures in care	0.277	70	90	89
<i>Tarao</i>	~1 year	F	26.5	110	Multiple seizures in care	0.347	120	100	113.3
<i>Daniela</i>	~1 year	F	23.5	114	Seizure and abnormal behavior	0.372	110	92	103
<i>Stern</i>	~1 year	F	24	122	Abnormal behavior	0.438	57	84	62.5
<i>Netz</i>	~1 year	F	21	112	Multiple seizures in care	0.403	60	68	60.5

rotate the animal unsupported for the remainder of the session.

Animals were scanned in ventral or dorsal recumbency, depending on size and additional procedures such as intravenous access to the subclavian vein. Dorsal recumbency was preferred for ease of vital signs monitoring in the magnet, however this position can be associated with hypotension in anesthetized sea lions (unpublished findings) and additional caution is warranted. Recumbency was found to have no significant effect on MRI scan quality, but patient registration must be either head-first prone or head-first supine for ventral or dorsal recumbency, respectively, to obtain the correct left-right assignment in images. For transit from the corridor into the scanner room it was necessary to temporarily disconnect the anesthesia tubing from the endotracheal tube, reconnecting once the gurney was wheeled into Zone IV and the vaporizer wheeled from the corridor into Zone III. The MRI patient bed height was set to match the gurney height so that the pad supporting the animal could be transferred to the patient bed directly, on top of the standard MRI bed padding. This placed the animal's head at an appropriate height for the receiver coil (Fig. 1). Once the sea lion was on the MRI patient bed, it was only necessary to slide the animal along the pad to center the brain in the receiver coil; this could be performed conveniently and safely at the magnet bore. Two nylon straps affixed to the MRI bed were used to secure the animal in case of seizures or unintended recovery from anesthesia while in the magnet. A pediatric fiber-optic pulse-oximetry sensor (Nonin 8600) was placed on the animal's tongue to measure heart rate (HR) and arterial blood oxygen saturation. However, intermittent signal meant that vital signs were primarily

determined by direct observation by a technician permanently stationed in Zone IV. Soft foam pads were placed snugly on either side of the animal's head, to provide hearing protection as well as maintain the head in the appropriate position in the receiver coil. We elected not to use ear plugs because of the potential difficulty removing them in emergency situations. Anesthesia was maintained at approximately 2% isoflurane in oxygen, the isoflurane level adjusted based on plane of anesthesia. Animals were intubated but breathed spontaneously. Hypercapnia was avoided with intermittent manual ventilation using a 3 L rebreathing bag. An MRI-compatible plastic disposable pediatric circle system with CO<sub>2</sub> absorber used as a semi-closed circle system and activated charcoal isoflurane scavenger (F/Air, AM Bickford, Wales Center, NY, USA) were mounted on a stand next to the magnet bore (Fig. 2). Monitoring included visual counts of respiratory rate and measurement of HR using a disposable plastic stethoscope (Proscope 665, American Diagnostic Corporation, Hauppauge NY, USA). Animals were cooled using the magnet bore fan and plastic bags of ice placed on the rear flippers. Lack of an MRI compatible thermometer meant that rectal temperature could only be taken outside Zone IV, before and after scanning.

At the completion of MR scanning, the gas line was temporarily disconnected from the endotracheal tube while the animal was transferred *via* the gurney to the transport crate in Zone II. Once in the crate, supplemental oxygen (100 %) was supplied until the animal recovered and was extubated. Respiratory rate and character were monitored during recovery. If not already reversed, medetomidine was reversed



**Fig. 1.** A 3-year-old California sea lion positioned on the patient table for scanning. Key features are 1: Receive-only neck coil. 2: Foam padding for head restraint and hearing protection. 3: Pad from the MRI compatible gurney, wrapped in plastic sheeting for hygiene. 4: Foam to position the muzzle. 5: Nylon strap for restraint. 6: Endotracheal tube and anesthesia line. 7: Pulse oximeter fiber-optic cable. 8: The base of the non-magnetic stand used to hold the anesthesia circle system.



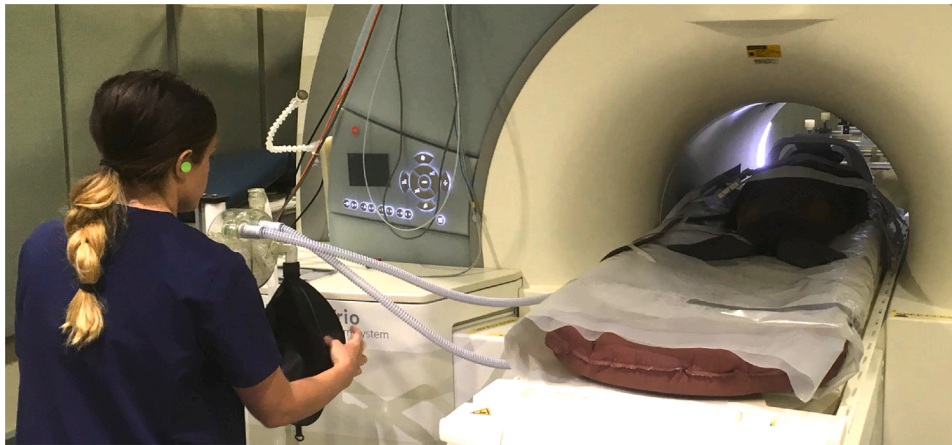


**Fig. 2.** A pediatric circle system with CO<sub>2</sub> absorber mounted to the left of the magnet bore, with the sea lion supported inside the magnet on the gurney pad (deep red, covered with plastic sheeting). An isoflurane scavenger (not visible) is connected below the anesthesia circle system. The veterinary technician, wearing hearing protection, remains in Zone IV to monitor vital signs directly and periodically assist ventilation manually via a 3 L rebreathing bag (black).

with atipamezole as described above. Ice was added to the crate as needed to support normal body temperature.

### 2.3. $T_1$ -weighted 3D MP-RAGE

Initial testing with a sagittal slab-selective 3D magnetization-prepared rapid acquisition of gradient echo (MP-RAGE) sequence, a conventional scan for human brain research, exhibited pronounced respiratory artifacts. The soft tissues of a sea lion's neck and lower jaw, which are both within the 3D field-of-view, move slightly with the chest during respiration. We therefore opted to change the prescription from sagittal to dorsal. This has the effect of swapping the phase encoding axes in the 3D acquisition. In the dorsal prescription, the first phase encoding direction is then left-to-right (L-R) and the second phase encoding direction is anterior-to-posterior (A-P) (equivalently ventral-dorsal). The slower k-space sampling A-P is more robust to throat movement at the respiratory rate. Dorsal 3D imaging with slab-selective excitation retains head-to-foot (H-F) frequency encoding, thereby permitting digital filtering of extraneous signal from the neck and upper body to eliminate aliasing. Remaining acquisition parameters for the MP-RAGE were adopted from the third phase of the Alzheimer's Disease Neuroimaging Initiative (ADNI-3) (Weiner et al., 2017). We have found the combination of repetition time, inversion time and flip angle used in ADNI-3 gives excellent gray/white tissue contrast in human brains. In accordance with standard clinical and research practice, we used the Prescan Normalize option to correct for the bias field imposed by the neck receiver coil. We opted to acquire standard 1.0-mm isotropic voxels, although we also tested 0.8-mm x 1.0-mm x 1.0-mm in two subjects. The higher resolution in the frequency encoding dimension is limited by gradient speed, while the 1.0-mm x 1.0-mm dimensions of the two phase-encoded dimensions were limited by scan time constraints. Acceleration using GRAPPA produced unacceptable artifacts (residual aliasing) with the 4-channel neck coil. On balance, the benefits of pushing beyond (1.0-mm)<sup>3</sup> were marginal for a scan of approximately 7-min duration.

### 2.4. $T_2$ -weighted 3D SPACE

Previous scanning of live sea lions has generally been conducted using 2D multiple spin echo sequences with two separate TEs per scan: a short TE of around 14 ms for a minimally T<sub>2</sub>-weighted scan (commonly referred to as proton density, PD contrast) for visualization of tissues, and a longer TE of around 100 ms for visualization of fluid-filled cavities. These scans have diagnosed the presence of gas-filled bubbles (Van Bonn et al., 2011, 2013) and have been used for volumetric

measurements of brain structures in living sea lions (Montie et al., 2009, 2010). An issue for quantification of small structures is the relatively thick slices used in 2D imaging, however. Voxel dimensions of 0.3-mm x 0.3-mm x 2.5-mm are typical. For research purposes, higher resolution through plane can be useful for tissue segmentation, e.g. for hippocampal volumes. In combination with a high-resolution MP-RAGE, a high resolution T<sub>2</sub>-weighted 3D scan may permit tissue typing and quantitative morphometry. We thus decided that 3D imaging was more likely to be useful in a longitudinal study of DOM toxicosis, and we focused on a long TE to compliment the structural information obtained in the MP-RAGE.

There are several approaches to multiple spin echo imaging, as reviewed by Mugler (2014). Multiple lines of k-space are acquired per excitation, but in general only one line of k-space is acquired per refocusing period. The effective TE, which by convention arises at the center of k-space, can be set to short or long values as desired. The number of refocusing periods (spin echoes) per excitation, the flip angle used for each refocusing pulse, and the effective TE at the k-space center all have profound effects on both image contrast and artifact levels. Imperfections in the refocusing radiofrequency (RF) pulses lead to complex pathways for magnetization, making artifacts likely. This has led to the development of variable flip angle (VFA) schemes across a single set of spin echo acquisitions, plus tactics to reduce artifacts that remain. On the Siemens platform, the SPACE sequence (Sampling Perfection with Application optimized Contrasts by using different flip angle Evolutions) has been optimized for 3D T<sub>2</sub>-weighted imaging of the brain. A remaining problem using VFA refocusing is produced by tissues which have short T<sub>1</sub> compared to brain, such as subcutaneous lipids. Short T<sub>1</sub> regions may appear mottled. The artifact, which arises from non-refocused signal, can be minimized using the principle of phase cycling of two otherwise identical scans. Alternatively, the relative contribution of non-refocused signal to properly refocused signal can be reduced by shortening the spin echo train, e.g. breaking it into two separate acquisitions. Either tactic doubles the overall acquisition time, however. We found that the phase-cycling approach with two averages at TE = 408 ms gave better image quality and preferable T<sub>2</sub>-weighted contrast than splitting the echo train into two halves, which limited the TE to a maximum of 256 ms.

In common with the MP-RAGE, we used a dorsal prescription with the first phase encoding axis set L-R to minimize respiratory ghosts. Given the historical use of 2D images with high in-plane resolution to depict the hippocampal formation in sea lions, we decided to acquire the smallest isotropic voxels possible. Voxel dimensions of (0.8-mm)<sup>3</sup> retained excellent contrast-to-noise ratio (CNR) and minimal artifacts. However, an issue with any T<sub>2</sub>-weighted 3D sequence is the long scan

duration. We used GRAPPA with an acceleration factor 2 in the second dimension (first phase encoding axis), and 5/8ths partial Fourier in the third dimension (second phase encoding axis) to bring the acquisition time down to 6-min. Residual aliasing artifacts from GRAPPA, even with the relatively poor performance of a 4-channel neck coil, are less of a problem than artifacts due to VFA refocusing of short  $T_1$  species, and a total scan time of 12-min would have been prohibitive.

## 2.5. $T_2$ -weighted 3D FLAIR

The  $T_2$ -weighted fluid-attenuated inversion recovery (FLAIR) scan is a mainstay of radiological imaging and is preferred for identifying edema and hippocampal atrophy, as may arise with DOM toxicosis. A standard clinical exam uses multi-slice 2D scans with the slice prescription established to cover regions of greatest interest. The inversion recovery (IR) delay, applied once per slice, limits the total number of planes that can be acquired in a reasonable amount of time. While the in-plane spatial resolution can be as high as 0.3-mm, the slice thickness is generally rather coarse and 3–5-mm slices are common. For a general examination, and for possible quantitative morphometric uses, a 3D scan permits *post hoc* slicing across any brain structure of interest, albeit at a lower resolution in two of three dimensions compared to the typical 2D scans.

We acquired a 3D  $T_2$ -FLAIR using a dorsal prescription to avoid respiratory ghosts, as above. The non-selective IR delay for CSF nulling and other parameters were set as for a human brain on the basis that we expect the  $T_1$  of CSF to be similar across mammalian species. Unacceptable residual aliasing artifacts with GRAPPA acceleration necessitated the use of 6/8ths partial k-space in the 3rd dimension to reduce the scan time, and this produces some Gibbs ringing artifact and partial smoothing in the third (A–P) dimension. As for the MP-RAGE, we utilized the Prescan Normalization option to correct the receive bias field.

## 2.6. Functional MRI

Cook et al. (2015) used fMRI under anesthesia - typically referred to

as resting-state fMRI because of the absence of an explicit task - to demonstrate altered hippocampal-thalamic connectivity in sea lions with hippocampal lesions likely caused by exposure to DOM. The prior study was conducted at 1.5 T and used an axial slice prescription. Given that the level of image distortion inherent to the echo planar imaging (EPI) sequence is expected to double at 3 T compared to 1.5 T, we opted to test all three cardinal slice prescriptions for BOLD contrast fMRI at 3 T. The voxel dimensions were fixed at  $(2.5\text{-mm})^3$ , which is approaching the maximum performance of the scanner hardware. For sea lion *Cronut*, the largest animal scanned so far, a dorsal prescription required only twenty-six 2.5-mm slices to cover the entire brain, whereas 30 and 35 slices were required to cover the brain in axial and sagittal prescriptions, respectively. The dorsal prescription thus offers the best coverage, *i.e.* shortest minimum TR.

We next considered the distortion and Nyquist ghosting inherent to the phase-encoded axis of the EPI pulse sequence. While H-F phase encoding produces symmetric distortions dorsally, L-R phase encoding allows faster gradient switching without violating the (human) peripheral nerve stimulation limits that are built-in to the scanner monitoring; these limits cannot be disabled in a scanner with FDA approval. Furthermore, for a 190-mm x 190-mm image the H-F phase encoding caused aliasing of signal from the neck to overlap the brain. It also produced Nyquist ghosts from both neck and muzzle aliased onto the brain (Fig. 3, left panel). By comparison, L-R phase encoding produced asymmetrically distorted brain images but there was no signal aliasing and the Nyquist ghosts did not overlap the brain (Fig. 3, right panel).

For BOLD-contrast we selected  $TE = 25$  ms. This is comparable to a  $TE$  used for human frontal or temporal lobe fMRI and approximates the  $T_2^*$  of brain tissues at 3 T. We did not attempt to quantify regional signal dropout but we noticed bilateral signal losses in cerebellum (Fig. 3, blue arrows) regardless of slice prescription, most likely because of the low position of the auditory bullae.

Selecting a suitable duration for task-free fMRI experiments requires some understanding of physiological noise sources, especially changes in arterial  $CO_2$  which for the human brain tends to fluctuate near to the frequency range most often studied in functional connectivity analyses

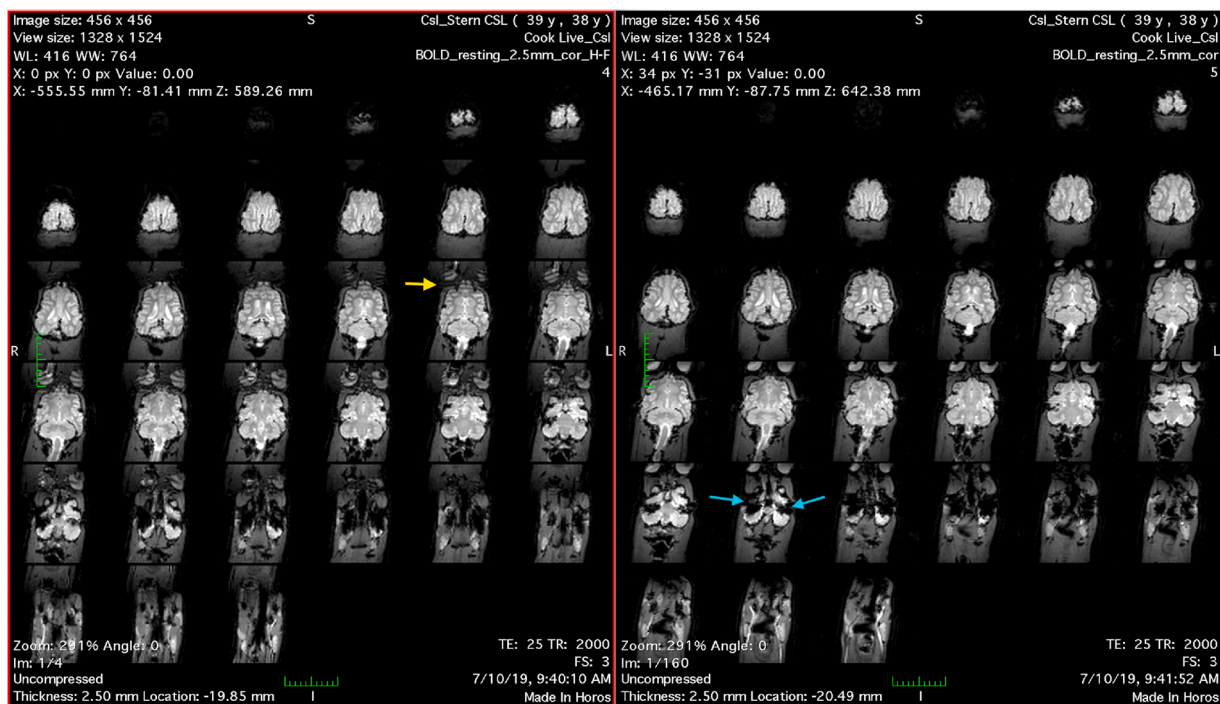


**Fig. 3.** Left: Dorsal sections of BOLD contrast EPI with phase encoding set H–F. A yellow arrow points out the banding artifacts caused by Nyquist ghosts aliased onto the eyes and frontal lobe. Right: Dorsal EPI with phase encoding set L–R, eliminating the banding artifact. Note that regions of dropout in cerebellum were present in all slice prescriptions and regardless of phase encoding direction. Blue arrows point out exemplars in the right panel.

(Tong and Frederick, 2010, 2014; Tong et al., 2013, 2019). We can record chest motion and HR, but given the intermittent reliability of pulse oximetry from the tongue and the limitations of respiratory models that derive arterial CO<sub>2</sub> changes from chest motion alone, we decided that we would instead rely upon data-driven de-noising methods. A 5-min scan comprising 160 volumes at TR = 2000 ms should provide adequate sensitivity to functional brain networks and the ability to characterize and remove physiological noise (Birn et al., 2013). We considered using SMS slice acceleration to decrease TR but were concerned about the possibility of misinterpreting residual aliasing artifacts which were visible in phantom tests with acceleration factors as low as two. On balance, we decided that the small sampling benefit from halving the TR was not worth the risk. We will revisit the possibilities afforded by SMS acceleration when a better RF coil might be available in place of the human neck coil, and once we have more experience of sea lion fMRI at 3 T.

## 2.7. Cerebral blood flow mapping

Arterial spin labeling (ASL) methods are well developed for human brain imaging, but to date they have not been applied to a pinniped. The principle of ASL is straightforward. Water in arterial blood is labeled magnetically as it transits the neck towards the head. The magnetically labeled water flows into the brain where it eventually exchanges with parenchymal water in the capillary bed, thereby changing the magnetization of the tissue water. An image captured after the labeled water has arrived at the tissue will reflect the total amount of labeled blood delivered, plus the amount of static water unperturbed by the label. This image is referred to as the labeled image, while the time elapsed from labeling to arrival at the tissue is the arterial transit time (ATT). A control image is required to account for the static signal component, and this is obtained by acquiring a second image with identical timing as the first but with the magnetic labeling of arterial water in the neck turned off. The difference of these two images then reflects the amount of arterial blood delivered to each location in the image. These difference images are often referred to as perfusion-weighted images (PWI). The voxel-wise CBF can then be computed from the PWI using models that include the experiment timing and certain assumptions concerning the magnetic label decay in transit and the partition coefficient of arterial blood water and tissue water.

Several ASL variants are available. For humans, the consensus view is that pseudo-continuous ASL (PCASL) is preferred, along with background suppression of static signal (Alsop et al., 2015). We have considerable experience with a background-suppressed stack-of-spirals PCASL sequence (Vidorreta et al., 2014, 2017) that uses unbalanced gradients during labeling to improve robustness to off-resonance effects and reduce labeling inefficiency due to pulsatility in the carotid arteries (Wu et al., 2007; Zhao et al., 2017).

Factors that can affect ASL sensitivity and CBF quantification include: (i) the (vascular) distance from the site of arterial blood labeling to the brain tissues, which determines optimal sequence timing, (ii) the blood velocity and pulsatility in the carotid arteries, which affects labeling efficiency, and (iii) the hematocrit, which affects the T<sub>1</sub> of the labeled blood as used in CBF quantification from raw PWI. In humans, a labeling period of 1800 ms provides a reasonable compromise between sensitivity and efficiency (Alsop et al., 2015). Timing of both the labeling period and the post-labeling delay (PLD) are important for accurate quantification of CBF. The PLD should be sufficiently long that all inverted blood water is delivered to the brain tissue prior to image acquisition. If the PLD is shorter than the slowest ATT then the CBF map can be biased by incomplete delivery of label. In the extreme, bright spots can appear in the final images, representing labeled blood still resident in arteries. On the other hand, the label decays with the T<sub>1</sub> of blood. Making the PLD too long will degrade the magnitude of the label unnecessarily, leading to low SNR in the PWI.

To adapt the stack-of-spirals PCASL sequence to sea lion brains, we

began by mapping the arteries using a time-of-flight (TOF) angiography sequence applied in the sagittal and dorsal directions, and displaying the maximum intensity projection (MIP) images (Fig. 4). While the left and right external carotids are quite far apart and follow the curvature of the neck, there is a location at which we could place the ASL labeling plane approximately perpendicular to the vessels. The labeling plane (Fig. 4, hatched bar) was located 90–105 mm caudal to the center of the 3D imaging volume (Fig. 4, yellow box), with the imaging volume centered over the brain. The longest distance of 105 mm was used on the largest sea lion scanned so far, 3-year-old *Cronut*, and is comparable to the distance used on an adult human brain, consistent with *Cronut* being approximately the same size as a large adult human. We used approximately 90 mm for the smaller yearling sea lions and note that in empirical tests on humans we have found that CBF values are reproducible even if the labeling plane location is varied by a few millimeters.

A labeling duration of 1800 ms and PLD of 1800 ms are preferred for the stack-of-spirals PCASL on a normal human brain. A longer PLD of 2000 ms is suggested when vasculature may be compromised, e.g. in stroke patients (Alsop et al., 2015). However, anesthetized sea lions tend to have a higher HR than awake humans - rates of 80–100 bpm are typical in sea lions - raising the possibility that arterial blood velocity and ATT might be appreciably faster in sea lions than humans and that shorter PLD might be warranted. We were also concerned that the hematocrit would be significantly higher than for typical humans, leading to shorter blood T<sub>1</sub>. Hematocrit values were determined after each scan, from blood drawn at the end of the session, but a value was not available for individuals while setting up the PCASL parameters. We therefore conducted empirical tests of the labeling duration (1200, 1500 and 1800 ms) and PLD (1200, 1500 ms) in different combinations across different animals, as scan time permitted. Unfortunately, several tests were contaminated with off-resonance spiral artifacts. We subsequently determined through tests of diffusion MRI (see below) that respiration was the most likely reason for frequency instability. Therefore, given that there is no prior knowledge on which to assess regional CBF in sea lions, we determined that the combination of 1800 ms labeling duration and 1200–1500 ms PLD gave the most reasonable CBF maps, i.e. fewest recognizable errors and greatest SNR, while emphasizing that the optimal timing will require further testing.

## 2.8. Diffusion imaging

Abnormal WM connectivity is expected in animals with hippocampal atrophy caused by DOM toxicosis. Using a diffusion imaging sequence developed specifically for scanning fixed, post mortem specimens, Cook et al. (2018) observed signs of WM pathology in the fornix as well as increased connectivity between the hippocampus and thalamus in sea lions with suspected DOM exposure, compared to brains from animals with no neurological signs of DOM toxicosis. Such a pattern has been observed previously in human patients with mTLE (Concha et al., 2010; Dinkelacker et al., 2015; Otte et al., 2012). Diffusion MRI has also been used to study chronic, low-level DOM exposure in live macaques (Petroff et al., 2019), and preliminary evidence indicates altered WM parameters in the fornix as well as the internal capsule.

The prior tractography study by Cook et al. (2018) was limited by hardware constraints to 1-mm isotropic voxels. Each brain was scanned at 3 T for approximately 8-h using a novel dMRI sequence that optimizes SNR for postmortem tissues with short T<sub>2</sub> (Miller et al., 2012; Foxley et al., 2014; Berns et al. 2015). For dMRI of anesthetized sea lions, however, total scan time was a more stringent constraint than either hardware limits or even image SNR. Our preliminary tests on post mortem specimens suggested that (2-mm)<sup>3</sup> resolution would be possible in an acceptable scan time using b = 1000s/mm<sup>2</sup> at TE = 93 ms and TR = 5800 ms. A partial Fourier scheme, 6/8ths of the phase encode direction, was used to reduce TE below 100 ms and maintain adequate SNR. Although higher spatial resolution and/or larger diffusion weighting were supported by the intrinsic SNR of the neck receiver coil,



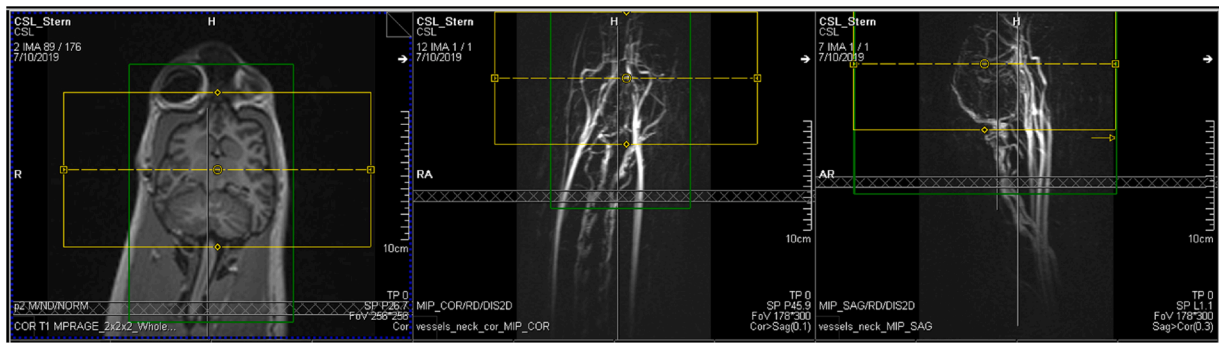


**Fig. 4.** Prescription of spatial parameters for ASL scan on yearling sea lion *Stern*, using a dorsal section through an MP-RAGE to determine the brain extent (left panel) and MIP of dorsal (center) and sagittal (right) TOF angiograms to allow correct placement of the labeling plane relative to the carotid arteries. The 3D imaging volume is depicted by the yellow box and the adjustment volume for magnetic field optimization is depicted as a green box. The labeling plane is shown as a horizontal cross-hatched rectangle located 90 mm below the centroid of the imaging volume.

either option would be prohibitively slow for a complete scan protocol of approximately 45-min. In preliminary tests, we also assessed GRAPPA with acceleration factor two in the phase encoding direction, to reduce the TE and halve EPI phase encode distortions, but we observed strong residual aliasing artifacts that might lead to false tracts. We considered SMS acceleration factor two but decided that, this being the first study of live sea lions with dMRI, we should first establish a performance baseline, again in case of residual aliasing (often termed “leakage” for SMS) presenting as false tracts.

The first task in a live animal was to determine optimal slice coverage and evaluate distortions, Nyquist ghosting and signal dropout, taking into consideration our earlier findings from the fMRI scan which also uses an EPI readout. We tested dorsal and sagittal prescriptions with the phase encoding direction set L–R and A–P, respectively. On 3-year-old sea lion *Cronut*, 40 2-mm dorsal slices were sufficient to cover the entire brain whereas 48 2-mm sagittal slices barely covered the brain. Neither prescription exhibited large regions of static signal loss, and spatial distortions were deemed not to be significantly different by inspection. In both cases, fat presaturation was highly effective at suppressing subcutaneous lipid and blubber signals so that Nyquist ghosts were weak and aliased outside the brain. However, the more efficient slice coverage offered by the dorsal prescription permitted a lower TR and more diffusion-encoded directions per unit acquisition time.

The first full dMRI data set was obtained on *Cronut*: 30 diffusion-weighted (DW) directions at  $b = 1000\text{s/mm}^2$  plus three  $b = 0$  images, one acquired before each block of ten DW images and used to improve eddy current correction. The total acquisition time was 3-min 17-sec. Raw image quality on initial inspection appeared to be quite good (Fig. 5). Subsequently, on yearling sea lion *Stern* we increased the number of DW directions to 64 plus six  $b = 0$  images, retaining  $b = 1000\text{s/mm}^2$ , for a total acquisition time of 6-min 52-sec. Finally, on yearling sea lion *Tarao* we attempted to change the acquisition strategy to a two-shell dMRI model (Wu and Alexander, 2007) using 50 DW images at  $b = 500\text{ s/mm}^2$  interleaved with 50 DW images at  $b = 1000\text{s/mm}^2$ , plus 11 images at  $b = 0$ , in an acquisition time of 10-min 50-sec, which is around the maximum duration permissible in the scan protocol for an anesthesia period not to exceed an hour. Inspection of the dMRI scans on *Tarao* revealed a previously overlooked problem. We noticed non-stationary signal voids in some but not all DW directions and in some but not all slices (Fig. 6). Assuming there was a problem with the directions used in the two-shell scheme, we acquired the 64 DW directions as used for *Stern*. Yet the non-stationary signal voids were still apparent, again in slice positions that were highly variable.

Subsequent review of the earlier data sets revealed that we had in fact encountered weaker, less frequent non-stationary signal voids in the DW images acquired from both *Stern* and *Cronut*. The initial suspicion

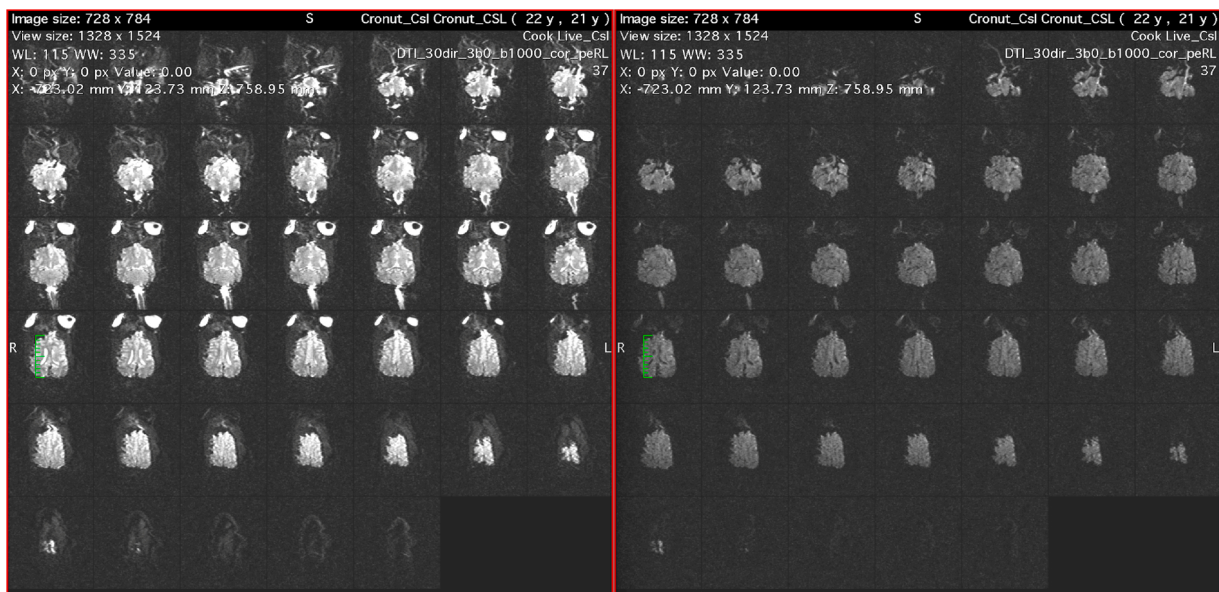


**Fig. 5.** Example diffusion-weighted images acquired from 3-year-old sea lion *Cronut* at  $b = 0$  (left) and  $b = 1000\text{s/mm}^2$  (right). Spatial resolution is  $(2\text{-mm})^3$ . For these dorsal slices the phase encoding is L-R. Note the distortion in the phase encoding direction, most easily recognized in the non-circular signal of the eyes.

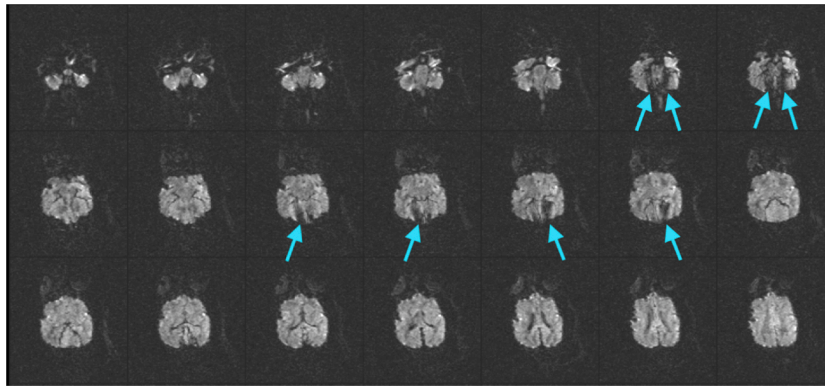


**Fig. 6.** Exemplar diffusion-weighted images from yearling sea lion *Taraa*, showing signal voids (arrows) that varied with slice position and dMRI direction in a random manner.

was of a mechanical resonance in the patient bed producing a DW direction-specific signal instability at  $b = 1000\text{s/mm}^2$ . While this is a known problem on Siemens Trio scanners (Gallichan et al., 2010; Berl et al., 2015), it has rarely been an issue on the BIC scanner and later tests suggested that mechanical resonances were not the likely culprit.

Gallichan et al. (2010) found that signal voids can arise because of phase shifts in the partial Fourier sampling used in the phase encoding dimension. Mechanical resonances are only one possible cause. Without a good explanation for the origin of the voids, we nevertheless tried schemes to alleviate them. A simple tactic is to reverse the polarity of the phase encoding gradient, e.g. from L-R to R-L. We tested reversed phase encode gradient polarity on yearling sea lion *Hammond* but aperiodic signal voids were still detected. We next tried  $b = 850\text{ s/mm}^2$  at TE = 90 ms and then  $b = 1500\text{s/mm}^2$  at TE = 100 ms, maintaining 6/8ths partial Fourier for both L-R and R-L phase encode polarity. Aperiodic signal voids persisted. The voids were most common in cerebellum, suggesting that perhaps the endotracheal tube was causing a signal instability via magnetic susceptibility gradients. Test scans were next acquired on *Hammond* with the endotracheal tube removed and a muzzle mask to maintain anesthesia, but the non-stationary voids were still observed.

At this point, we realized that the most likely explanation was a shift of the resonance frequency caused by inflation of the animal's chest with the intermittent manual ventilation. Modulation of the main magnetic field across the brain during respiration is a well-known source of physiological variance in human fMRI scans (Van de Moortele et al., 2002). In the case of our dMRI scans, the frequency shift due to movement of the sea lion's chest may be sufficient to produce a phase shift in the partial k-space and cause the signal voids. This leaves two options: exchange partial Fourier for GRAPPA acceleration to maintain the TE below 100 ms and risk exchanging one artifact type for another, or change the procedure for monitoring and ventilating the animal during the dMRI scan. In future tests, we will ventilate manually only during  $b = 0$  scans and we will include additional  $b = 0$  scans if extra time is required to complete the procedure. Despite a few weak signal voids, we decided to process the 64-direction data set from *Stern* and assess the tractography pipeline for basic structural connectivity estimation.

### 3. Results

#### 3.1. Anatomical scans

Examples of high quality MP-RAGE, SPACE and T<sub>2</sub>-FLAIR images are shown in Figs. 7–9, respectively. Gray matter (GM) and WM are clearly differentiated in the MP-RAGE; CSF appears dark, as in the human brain (Fig. 7). The CSF is hyperintense in the SPACE image, with GM brighter than WM (Fig. 8). In the T<sub>2</sub>-FLAIR (Fig. 9), normal tissue appears relatively isointense and CSF is dark. In some animals with suspected DOM toxicosis, hippocampal gliosis was detected easily in the T<sub>2</sub>-FLAIR, with

corresponding atrophy evident in the MP-RAGE and SPACE scans (data not shown). An experienced ACVR board-certified veterinary radiologist (SD) determined that a full clinical read was feasible using the 3D scans.

Left and right hippocampi were segmented separately and volumes were obtained using the open-source software *3D Slicer* ([www.slicer.org](http://www.slicer.org)) for sea lion *Stern* using T<sub>2</sub> images (Fig. 10). For segmenting hippocampal GM, an oblique orientation was selected perpendicular to the septo-temporal (longitudinal) axis of the hippocampus. This orientation has been used in prior hippocampal volumetry with sea lions (Montie et al., 2009, 2010; Cook et al., 2015), and allows clear contrast between the caudoventral boundaries of hippocampal GM, particularly in the *cornu Ammonis* (CA), and the CSF of the lateral ventricles. Tissue segmentation was cross-referenced on each oblique slice against a sagittal view. Hippocampal tracings included the CA subfields, dentate gyrus and alveus, as well as a portion of the subiculum. There are no clear anatomical criteria for distinguishing subiculum from CA in the sea lion. Septal and temporal boundaries of the hippocampus were based predominantly on the visible extension of hippocampal tissue in the sagittal view. Hippocampal tissue was clearly visible two to three slices temporal to the last oblique slice in which the cerebral peduncles could be seen. The septal boundary was just dorsal to the dorsal boundary of the splenium of the corpus callosum. At this level in the oblique images the sea lion hippocampus appears flattened, as in primates. Sea lions do not have a large dorsal extension of CA as seen in canids and rodents.

The lateral boundary of the hippocampus was determined by the lateral ventricle of the temporal horn. Alveus was included where it could be clearly distinguished, but fimbria was not. The medial boundaries were set as the medial-most extension of subicular cortex. Rostroventral boundaries were defined by an arbitrary straight line connecting the most medial portion of subiculum to the most medial portion of parahippocampal tissue dorsal to parahippocampal gyrus.

Hippocampal volumes were computed using the *segmentstatistics* module in *3D Slicer*. Left hippocampus was  $580.2\text{ mm}^3$ . Right hippocampus was  $367.3\text{ mm}^3$ . The notable difference in volumes matches radiological assessment of *Stern*'s images, which suggest enlarged ventricles around the CA of the right hippocampus. Hippocampal volumes measured here are on the lower end of the range of previous measurements in sea lions. The differences may be due to the young age of the animal and potential bilateral atrophy. In addition, unlike previous segmentations, high-quality 3D imaging allowed us to carefully trace in an oblique plane while also using the sagittal orientation to carefully identify the longitudinal boundaries of hippocampal tissue. Montie et al. (2010) previously measured hippocampal volumes in six sea lions in the  $\sim 700\text{--}1000\text{ mm}^3$  range using 2D T<sub>2</sub>-weighted imaging with 0.3-mm x 0.3-mm resolution in-plane and 2.5-mm slices. Follow-up work by Montie et al. (2012) using the same 2D acquisition identified similar volumes in fifteen further sea lions. Cook et al. (2015) measured right and left hippocampus in 30 sea lions using 2D T<sub>2</sub>-weighted imaging with



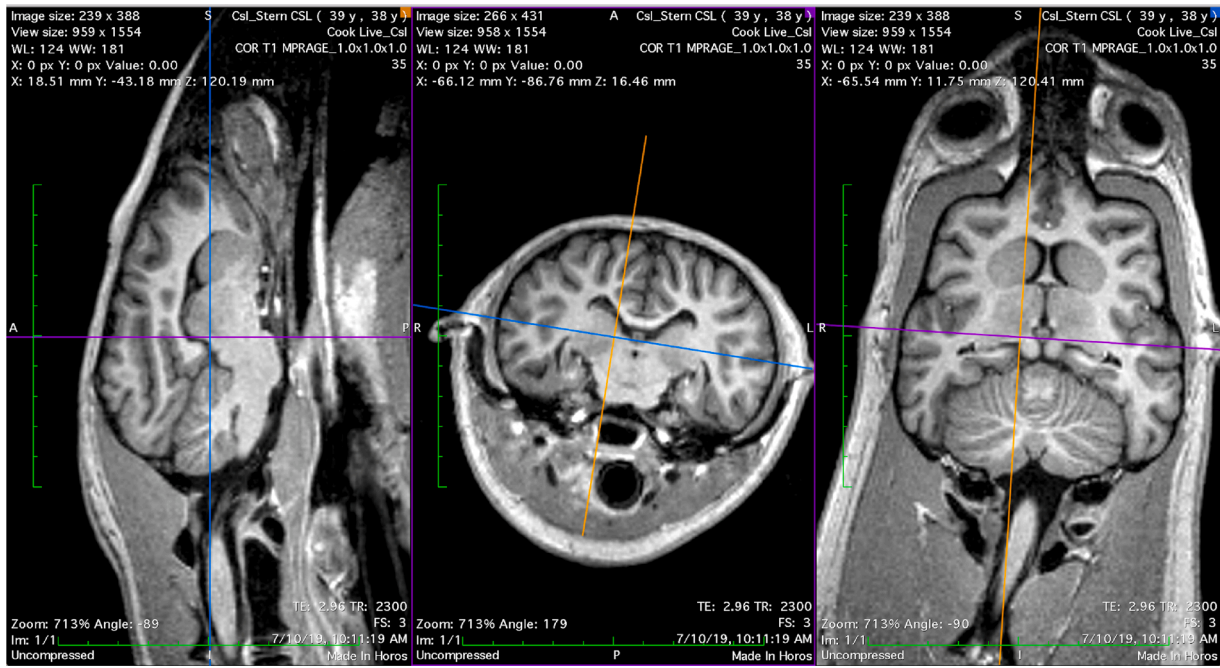


Fig. 7. T<sub>1</sub>-weighted 3D MP-RAGE images obtained on yearling sea lion *Stern*. Image orientation terminology: Left panel = sagittal, middle panel = transverse, right panel = dorsal.

0.695-mm x 0.695-mm resolution in-plane and 2.0-mm slices, and found volumes ranging from ~400 to 900 mm<sup>3</sup>. Some of these animals had severe hippocampal atrophy. General segmentation criteria were similar in all cases. In the current work, with isotropic 3D imaging and elimination of CSF signal using FLAIR, we delineated all likely hippocampal tissue along the septotemporal axis but medial hippocampal tissue boundaries were not always clear. Cook et al. (2018) measured hippocampal volumes from high-resolution post mortem MRI (0.6-mm x 0.6-mm x 0.5-mm) and found higher volumes, ranging from ~900 to 1800 mm<sup>3</sup>. Given the limited prior work describing sea lion hippocampal anatomy, the present imaging protocols will allow us to carefully

determine and standardize future measures using anatomical criteria.

### 3.2. Functional MRI

Functional connectivity analysis was conducted on data obtained from sea lion *Tarao*. Data preprocessing was carried out using a combination of manual steps and FEAT (FMRI Expert Analysis Tool) Version 6.00, part of FSL (FMRIB's Software Library, [www.fmrib.ox.ac.uk/fsl](http://www.fmrib.ox.ac.uk/fsl)) (Woolrich et al., 2001). The following corrections were applied in this order: (i) volume realignment for motion correction using MCFLIRT (Jenkinson et al., 2002); (ii) slice-timing correction using Fourier-space

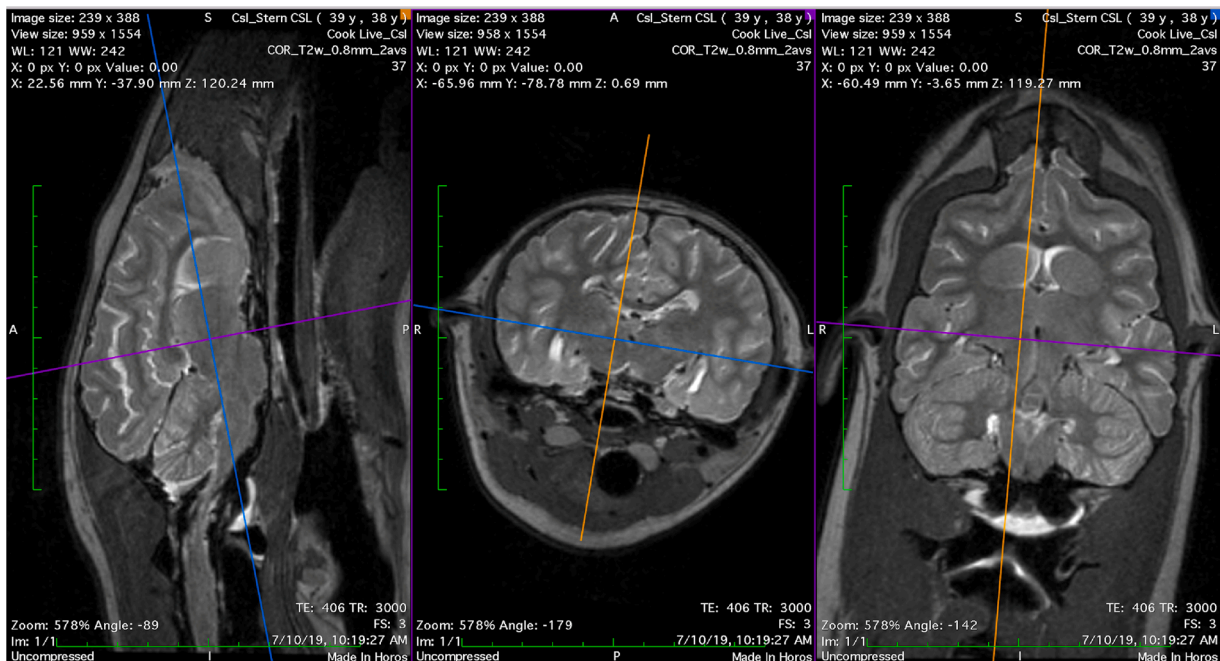


Fig. 8. T<sub>2</sub>-weighted 3D SPACE images obtained on yearling sea lion *Stern*.



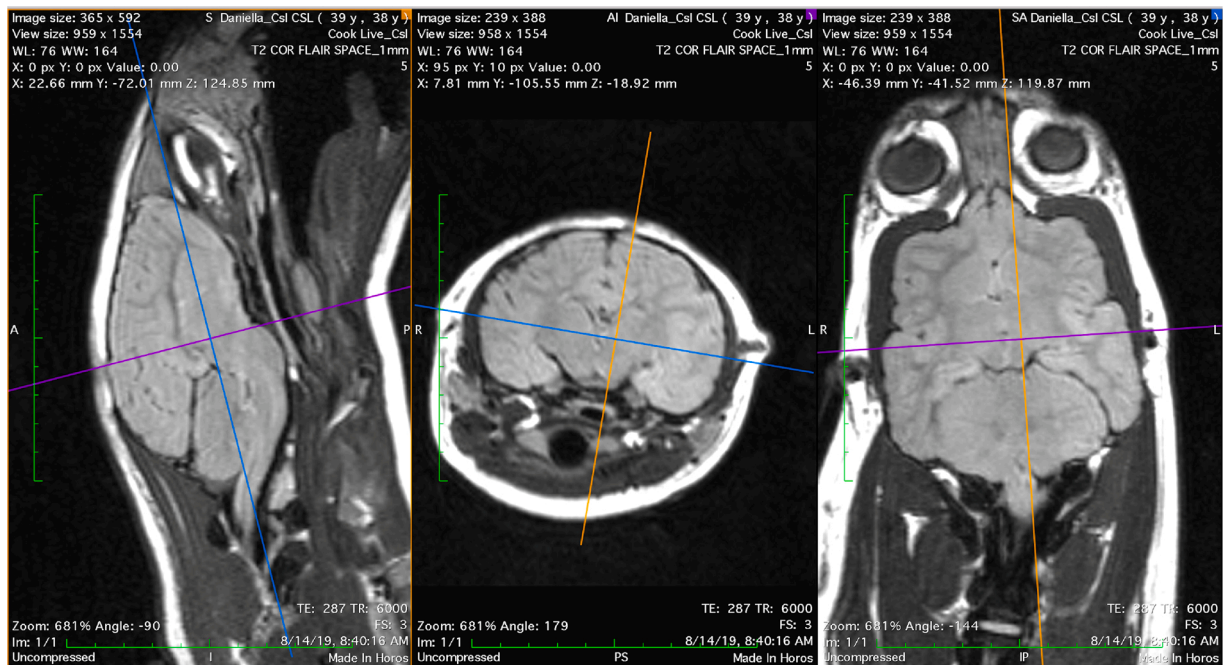


Fig. 9. T<sub>2</sub>-weighted 3D FLAIR images obtained on yearling sea lion *Daniela*.

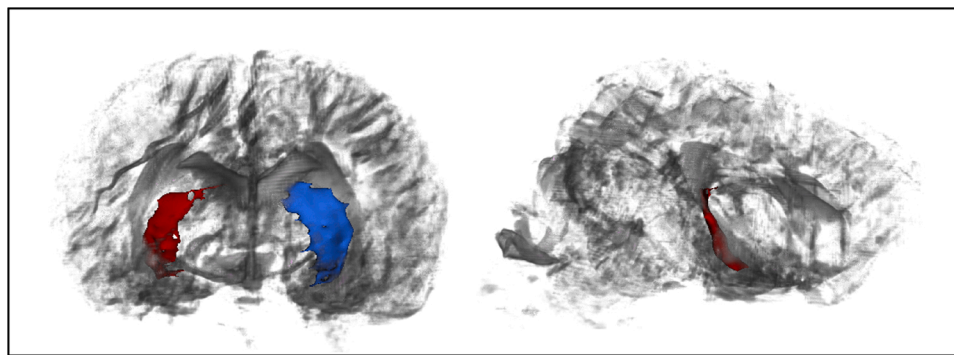


Fig. 10. Left: Transverse render of right (red) and left (blue) hippocampal segmentations in a semi-transparent brain volume. Right: Sagittal render of right hippocampal segmentation. Both from sea lion *Stern*.

time-series phase-shifting; (iii) non-brain removal by multiplication with a hand-drawn brain mask; (iv) spatial smoothing using a 2-mm Gaussian kernel; (v) grand mean intensity normalization of the entire 4D dataset by a single multiplicative factor; (vi) high-pass temporal filtering (Gaussian-weighted least-squares straight line fitting, with  $\sigma = 75.0$ -sec).

Next, we sought to assess systematic effects of the manual ventilation procedure using an independent component analysis (ICA)-based exploration of the time series with automatic dimensionality estimation using MELODIC (Beckmann and Smith, 2004). Independent components were manually evaluated with the grading tool *PICACHOOSE* (<https://github.com/bbfrederick/picachoser>) (Frederick, 2020) to flag artefactual components at the manual ventilation rate. Fourteen out of 21 independent components found by MELODIC exhibited well defined, pseudo-periodic maxima across the time series every 50–60 s. The maxima had differing shapes and temporal lags for each IC but maintained the same frequency of  $\sim 0.02$  Hz. The spatial locations of the ICs were most prominent in inferior brain regions and locations consistent with large arteries, suggesting a vascular origin for the signal changes (Fig. 11). Non-stationary blood gas concentrations, particularly arterial CO<sub>2</sub>, modulate arterial tone in a manner that produces concomitant BOLD signal changes (Wise et al., 2004). The 14 components assigned as

artifacts of the manual ventilation were removed from the preprocessed data using “fsl\_regfilt” prior to further analysis. In total, these components accounted for 38.4 % of total signal variance.

For functional connectivity analysis of the cleaned data, a dorsal left hippocampal mask was created on the T<sub>1</sub>-weighted structural image in FSLEyes, following Cook et al. (2015). White matter and CSF masks were also generated from the structural image using FSL’s FAST (Zhang et al., 2001), and thresholded at  $p(\text{tissue}) > 0.95$ . Hippocampal, WM and CSF masks were registered into native functional space using FSL’s FLIRT (Jenkinson and Smith, 2001; Jenkinson et al., 2002). A time course from the pre-processed data was extracted from each registered mask, computed as the average BOLD signal at each time point for each region.

Temporal correlation analysis was conducted in FSL’s FEAT using the general linear model with the dorsal left hippocampal time course as the primary covariate. The WM and CSF time courses (Behzadi et al., 2007) plus the six realignment parameters (three translations, three rotations) were included as nuisance covariates to mitigate physiological noise and motion. Resulting correlation maps were registered to anatomical space for display, to indicate areas with highest functional connectivity with the dorsal left hippocampus (Fig. 12).

As in Cook et al. (2015), there was significant co-activation with the dorsal hippocampus in dorsal thalamus and the caudate nuclei (Fig. 12,

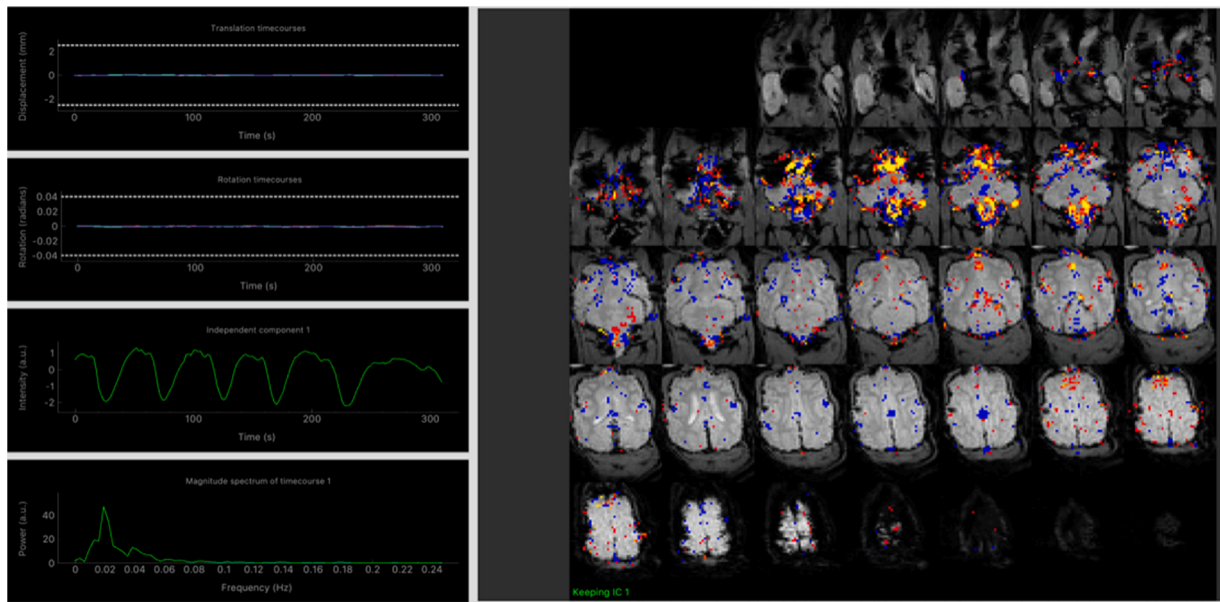


**Fig. 11.** The first of 14 independent components identified using MELODIC independent component analysis, sorted using *PICChooser*. The third row of the left-hand column shows the time series corresponding to the colored voxels displayed in the right panel. The six maxima of the time series correspond to the manual ventilation, approximately one per minute. The brightest voxels arise at the base of the brain and brainstem and around the locations of large vessels, especially arteries. From sea lion *Tarao*.

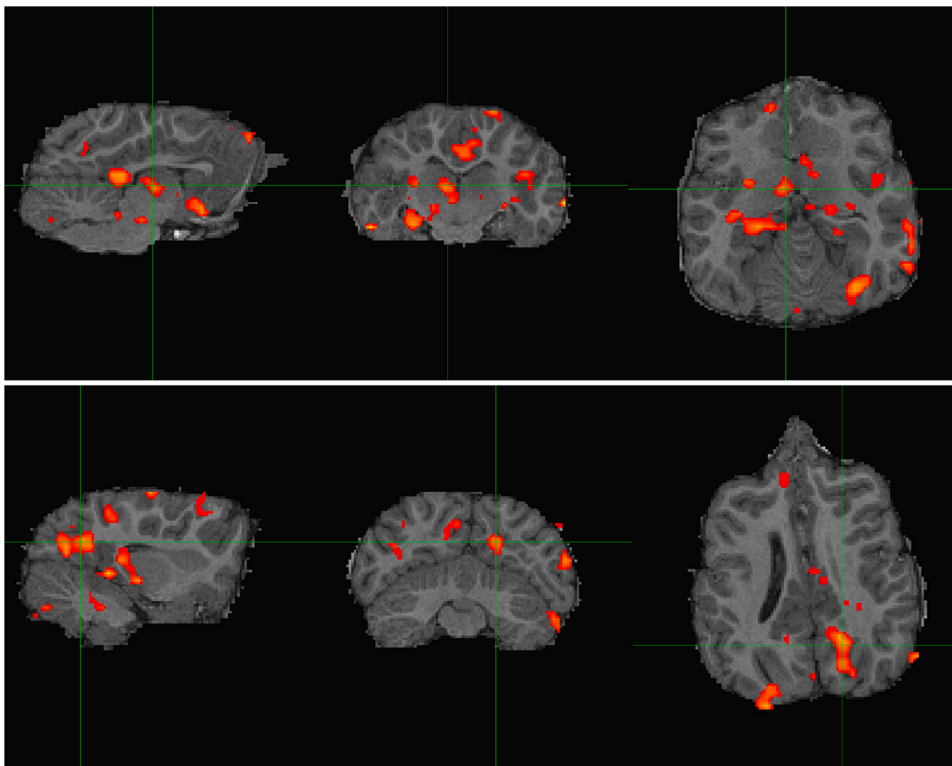


**Fig. 12.** Resting-state connectivity analysis for sea lion *Tarao* presented in, from left to right, sagittal, transverse, and dorsal planes. Top: Z-score map thresholded at  $Z > 3.1$  computed from a dorsal left hippocampal seed. Strongest correlation was observed in the cingulate cortex and dorsal thalamus (cross hairs), ventral caudate nuclei, and right hippocampus (contralateral to the seed). Bottom: Another view of connectivity with the dorsal left hippocampal seed, presenting an area of caudal cortical activation potentially overlapping with visual processing regions (cross hairs).

top). This is in line with established evidence regarding hippocampal connectivity in humans and other mammals (Stein et al., 2000). Work in human epilepsy indicates that hippocampal-thalamic pathways can be affected by chronic seizures (Barron et al., 2014). Contralateral hippocampal co-activation was also observed. Unlike in Cook et al. (2015), however, there was significant correlation in posterior dorsal cortex, potentially in a visual processing region (Fig. 12, bottom), which is in line with evidence on hippocampal connectivity in rodents and humans

(Eichenbaum, 2000; Lavenex and Amaral, 2000; Ranganath et al., 2005). Unfortunately, the presence of high co-activation in the brainstem and parts of the lateral ventricles suggests the data are affected by residual physiological noise. Manual ventilation produces large magnetic field variations over the brain from the magnetic susceptibility of the abdomen, as well as the possibility of large direct motion of the head, and the de-noising tactics employed here were likely insufficient. Future analyses might include covariates derived from direct physiological

monitoring, such as the motion of the chest which can be recorded with a plethysmograph belt, and principled removal of non-stationary arterial CO<sub>2</sub> effects (Tong et al., 2019).

### 3.3. Cerebral blood flow mapping

Using a 3D stack-of-spirals PCASL sequence, we tested different combinations of labeling duration (1200, 1500 and 1800 ms) and PLD (1200, 1500 ms) across different individuals using fast (1-minute), low SNR scans (data not shown). The perfusion-weighted difference images suggested that reasonable CBF might be obtained using an 1800 ms labeling period and 1200–1500 ms PLD. As a test case, the ASL data from

sea lion *Cronut* (1800 ms labeling period, 1200 ms PLD, 2-shot interleaved spiral acquisition with 3.8 mm<sup>3</sup> voxels, 3-minute acquisition time) was analyzed following established methods for determining CBF in the human brain. The full label and control time series was first realigned to mitigate any motion. Regional CBF was then computed using single compartment kinetics (Alsop et al., 2015). The model used an assumed brain/blood partition coefficient of 0.9 and labeling efficiency of 0.72 (Dolui et al., 2019), determined based on experiments conducted in normal humans. The  $T_{1,\text{blood}} = 1.74$  s was calculated from the relationship  $1/T_1 = 0.62 \cdot \text{Hct} + 0.28$  (Li et al., 2017) using a hematocrit value of 0.47 obtained from blood drawn under anesthesia during the scanning session.

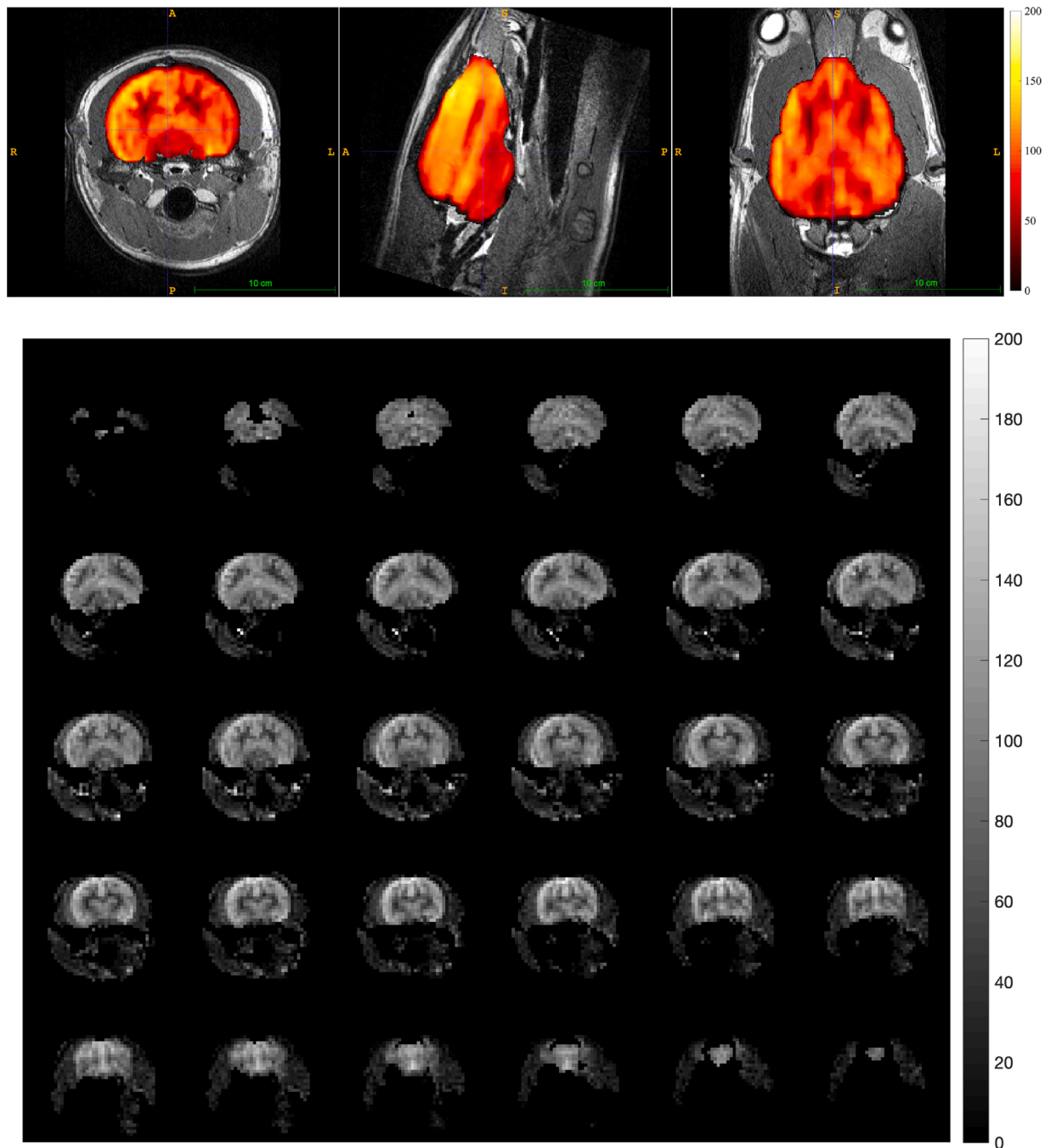


**Fig. 13.** Cerebral blood flow maps obtained from 3-year-old sea lion *Cronut* using a 2-shot stack-of-spirals PCASL sequence with 1800 ms labeling period and 1200 ms post-label delay. Units are mL blood/100 g tissue/minute. Top: Three plane view. The CBF map is overlaid on the T<sub>2</sub>-weighted anatomical scan. Images are, left to right, in the transverse, sagittal, and dorsal planes. Bottom: CBF maps in transverse 2D view.



A whole brain mask was determined from *Cronut*'s 3D T<sub>2</sub>-weighted image using FSL's *BET* followed by small manual adjustments to accommodate species differences. The masked CBF map is shown overlaid on the T<sub>2</sub>-weighted anatomical scan in Fig. 13. The gross features in the CBF map are consistent with observations in the normal human brain, i.e. CBF in GM is approximately three times greater than in WM, reflecting the greater metabolic rate of cell bodies than axons. Despite possible species differences and the effects of anesthesia, it is instructive to compare the global mean CBF found for *Cronut* with typical human data obtained using ASL. The mean global CBF in *Cronut* was 81.3 mL/100 g/min. This compares favorably with values of around 80 mL/100 g/min measured in 8-year-old humans (Satterthwaite et al., 2014).

### 3.4. Diffusion imaging

The dMRI data obtained on sea lion *Stern* had the fewest non-stationary signal voids that could be determined by inspection, and these images were submitted for tractographic analysis. We noted only four possible signal voids, all confined to the cerebellum, in the entire dMRI data set for *Stern*.

Processing of dMRI data was performed using FDT (FMRIB's Diffusion Toolbox, Oxford University, UK). Images were first converted from DICOM to NIFTI format using *DCM2Nii*. The six  $b = 0$  images were co-registered and averaged to serve as a structural reference for the dMRI data. The non-canonical orientation of the sea lion's head during imaging required a correction to the DW vectors produced by the scanner: the  $y$  and  $z$  axes were swapped, then the signs were reversed for the  $x$  and  $y$  axes. The results of the corrections were checked carefully in all three planes using FA maps with voxel-wise principal diffusion directions overlaid, all generated via FSL's *DTIFit* tool. Diffusion data were then registered to the average  $b = 0$  image. A brain mask generated by FSL's *BET* tool, with manual editing, was created from the average  $b =$

0 image and used to skull-strip the registered diffusion data. Simultaneous eddy current correction and volume realignment for motion correction was then performed on all DW images using FSL's *eddy* tool. Corrected images were used henceforth.

Images of FA and MD were produced using FSL's *DTIFit* tool. This utility assumes a tensor model for the underlying diffusion (Basser et al., 1994). For tractography, however, we used a probabilistic model to estimate local diffusion parameters in each voxel with FSL's *bedpostx*, a Bayesian estimation probabilistic diffusion model which attempts to account for crossing fibers by Markov Chain Monte Carlo sampling to build up distributions on diffusion parameters within each voxel.

The output from *bedpostx* (Fig. 14, top) was used to perform probabilistic fiber tracking using FSL's *probtrackx* (Behrens et al., 2003, 2007) and deterministic fiber tracking using DSI Studio (<http://dsi-studio.labsolver.org/>). As in Cook et al. (2016), we traced the crus and pillar of fornix tracts. Hand-drawn anatomical seeds for these tracings were created in FSL's *FSLView* directly in DTI space, over FA maps. The seed was placed in the crus of the fornix and situated in high FA apparent WM with clear rostro-caudal diffusion directionality per an overlaid diffusion vector map. The seed was just ventral to the corpus callosum, and the rostral boundary was caudal to the ventral turn of the rostral fornix. Termination masks were also created, one in the dorsal plane ventral to the splenium and one in the transverse plane caudal to the septum, which terminated any apparent tracts entering the corpus callosum and septum pellucidum, respectively. Probabilistic tracing was conducted with 5000 streamlines per seed voxel, a step length of 0.5-mm, and a standard curvature threshold of 80 degrees. The resulting tracts at 1% threshold clearly demarcated the fornix.

Both probabilistic and deterministic fornix tracings in the current study were in line with previous postmortem DTI analyses in sea lions (Cook et al., 2018), suggesting that *Stern*'s dMRI data were acceptable despite the aperiodic signal voids noted in cerebellum. Fornix was clearly identified in FA maps based on anatomical criteria with principle

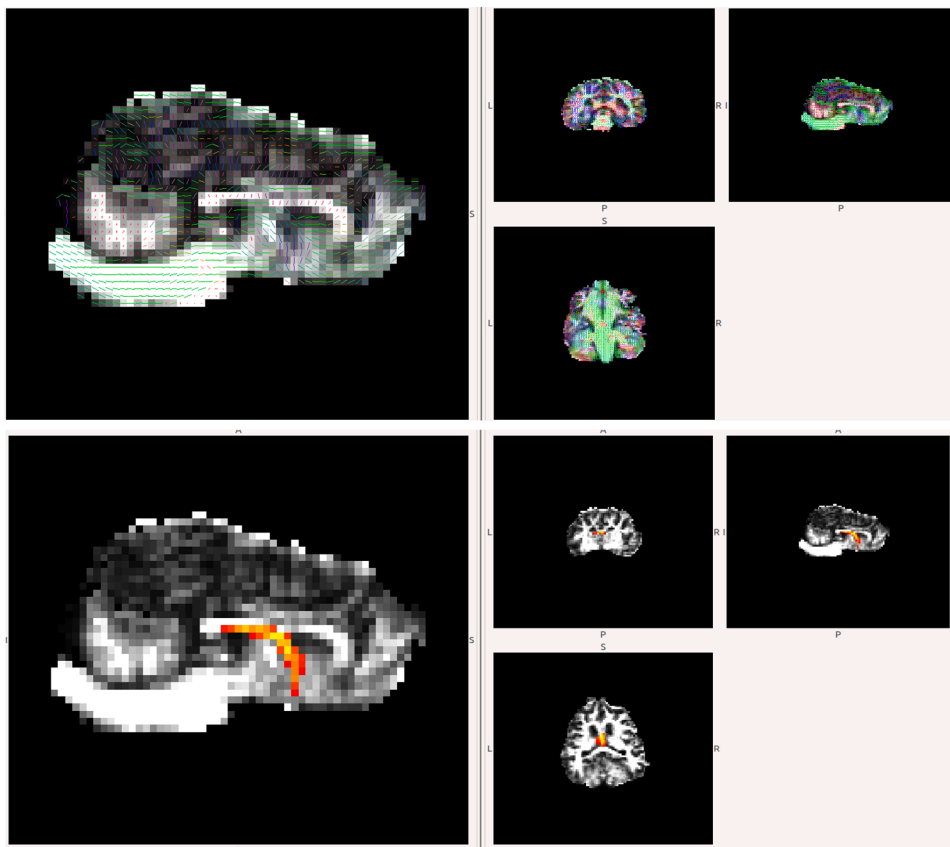
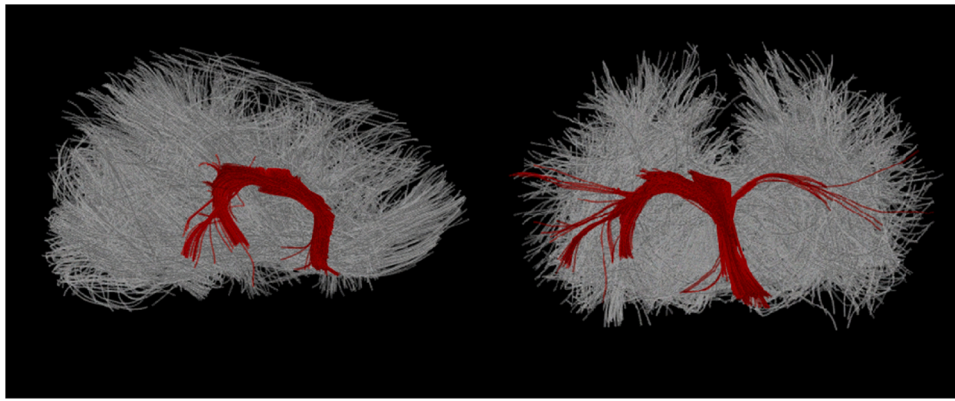


Fig. 14. Top: Voxel-by-voxel representation of principle diffusion directions in sagittal (left, large) and all three canonical (three right, small) planes, shown in diffusion space/resolution. Diffusion data are overlaid on a  $b = 0$  image. Each voxel has a line and color indicating principle water diffusion direction. Green voxels are rostro-caudal, red voxels left-right, and blue voxels dorsal-ventral. Bottom: Hippocampal fornix traced from a bilateral fornix pillar seed, at 1% threshold of total streamlines. Data from sea lion *Stern*.



**Fig. 15.** A deterministic tracing of hippocampal fornix produced from a fornix pillar seed analogous to that used in Fig. 14, overlaid on a whole brain rendering of all fibers, in the sagittal (left) and transverse (right) views. Deterministic tracing does not use thresholding but termination masks were used dorsal to the dorsal fornix and caudal to the caudal-most portion of fornix. Data from sea lion *Stern*.

diffusion maps benefitting seed placement (Fig. 14, bottom). The apparent lack of traceable forniceal WM in the left hippocampus using deterministic tractography (Yeh et al., 2013) may be indicative of damaged tissues (Fig. 15). In Cook et al. (2018), fornix FA values were significantly lower in animals with diagnoses of DOM toxicosis and hippocampal atrophy, as also reported in human patients with mTLE (Concha et al., 2010). Deterministic and probabilistic tracing rely in part on FA thresholds voxel-by-voxel. However, partial volume effects around ventricles has been identified as a confound in DTI of the fornix previously (Kuroki et al., 2006). Whether the present results are representative of WM pathology will require resolution of the signal void issue and, ideally, a comparison of *in vivo* to post mortem dMRI from the same brain to confirm.

#### 4. Discussion

We have developed a research MRI protocol suitable for studying the brains of California sea lions suspected of suffering DOM toxicosis. A list of recommended scan parameters appears in Table 2, although we note that the dMRI and ASL scans may be further refined with additional tests. The scan protocol should be suitable for sea lions over a range of sizes, having been developed on subjects of 21–96 kg. Our long-term goal is to study the brain development of sea lions exposed *in utero* to DOM, from 6 months to 4 years of age. Beyond four years it is likely that

male subjects would be too large for our MRI scanner. The availability of a wide-bore scanner with a patient bed rated to 250 kg would permit scans of slightly larger animals, assuming procedures for safe animal handling to and from the MRI bed.

Clinical evaluation of DOM toxicosis has used 2D MRI scans previously. We opted to use 3D anatomical scans because these permit improved tissue volume measurements, as required for a quantitative longitudinal study of changes following DOM toxicosis, and for arbitrary re-slicing *post hoc*. An experienced ACVR-board certified veterinary radiologist (SD) confirmed the utility of the 3D scans for clinical purposes. Beyond DOM toxicosis, we predict that the 3D scans would permit clinical discrimination of brain pathologies such as tumors, hemorrhages, and the presence of gas bubbles.

The greatest technical challenge to high quality images was caused by respiration, mainly the requirement to manually ventilate the animal periodically to avoid hypercapnia. Respiration negatively affected all scan types when using standard human parameters, necessitating scan-specific tactics to ameliorate. In 3D anatomical scans, respiration presented a challenge due to the orthogonal orientation of the sea lion's brain relative to a supine human, and the comparatively large volume of tissue in a sea lion's throat; normal respiration produces very small movements of throat signal in humans. A comparable problem in human imaging is swallowing, which produces large excursions in both A–P and H–F directions and would cause analogous errors were it to occur with

**Table 2**  
Recommended MRI scan parameters.

Scan type	Sequence type	TR	TE	Spatial resolution (mm)	Additional parameters	Acquisition time	Notes
T <sub>1</sub> -weighted anatomical	3D MP-RAGE	2300 ms	2.96 ms	1.0 × 1.0 × 1.0	T <sub>INV</sub> = 900 ms, non-selective inversion. Excitation flip angle = 9 degrees.	7 m 23s	<sup>a</sup>
T <sub>2</sub> -weighted anatomical	3D SPACE	3000 ms	406 ms	0.8 × 0.8 × 0.8	Turbo factor = 141, slice turbo factor = 2.	6 m 02s	<sup>b</sup>
T <sub>2</sub> -weighted anatomical with fluid attenuation	3D FLAIR-SPACE	6000 ms	287 ms	1.0 × 1.0 × 1.0	T <sub>INV</sub> = 2200 ms, non-selective inversion. Turbo factor = 101, echo trains per slice = 2.	8 m 26s	<sup>c</sup>
BOLD-weighted functional MRI	2D GRE-EPI	2000 ms	25 ms	2.5 × 2.5 × 2.5	No. of volumes = 160. Excitation flip angle = 65 deg. Slice order = descending. Read bandwidth = 2192 Hz/pixel, echo spacing = 0.52 s.	5 m 22s	<sup>d</sup>
CBF mapping	3D stack-of-spirals PCASL	4600 ms	8.7 ms	3.0 × 3.0 × 3.0 (or 3.8 × 3.8 × 3.8)	Labeling duration = 1800 ms, post-labeling delay = 1200–1500 ms	4m 37s	<sup>e</sup>
Diffusion MRI	DW-SE-EPI	5800 ms	93 ms	2.0 × 2.0 × 2.0	64 directions at b = 1000s/mm <sup>2</sup> plus six b = 0 images	6 m 58s	<sup>f</sup>

<sup>a</sup> Excellent gray/white matter contrast; useful for quantitative morphometry.

<sup>b</sup> Good tissue contrast & visualization of CSF. Also shows edema & gliosis.

<sup>c</sup> Excellent identification of pathology, especially edema & gliosis. Can be used for quantitative morphometry.

<sup>d</sup> FA < 65 deg would reduce physiological artifacts without compromising intended BOLD contrast.

<sup>e</sup> For 3.0 mm or 3.8 mm voxels a 4- or 2-shot segmented spiral readout is used, respectively. Optimal PLD may vary depending on animal size/age.

<sup>f</sup> Requires 6/8ths partial Fourier to keep TE < 100 ms, which may enhance sensitivity to respiratory artifacts.

the frequency of respiration.

Our test of functional connectivity from fMRI yielded results at 3 T that matched prior results obtained at 1.5 T, with dorsal thalamus and dorsal caudate co-activated with a dorsal hippocampus seed. In general, the magnitude of BOLD contrast is expected to increase with main magnetic field strength, offering more sensitivity at 3 T, but this advantage manifests only if physiological changes unconnected to neurovascular coupling can be minimized (Liu, 2016; Wald and Polimeni, 2017). We observed a major perturbation consistent with manual ventilation. Many regions, notably arteries in the inferior slices, fluctuated at the pseudo-periodic rate of the manual ventilation and exhibited high signal variance, strongly suggesting a BOLD signal change due either to non-stationary arterial CO<sub>2</sub> (Tong and Frederick, 2010; Tong et al., 2019) and/or non-stationary deoxyhemoglobin concentration in arterial blood whenever SaO<sub>2</sub> departs from the assumed value of 100 % (Aso et al., 2019). Such respiration-induced changes are typical in humans. The issue here is the magnitude of the response to intermittent manual ventilation. In future, during fMRI acquisition we will attempt a more regular manual or mechanical ventilation with smaller volumes, to better resemble normal ventilation. A scripted ventilation routine will also give us ground truth knowledge to improve identification and separation of respiratory effects from ongoing brain activity.

We do not yet know whether manual ventilation affected the CBF map measured with ASL, via the well-known vasodilative effects of arterial CO<sub>2</sub>. In future tests, we will compare CBF maps produced with large volume, low rate ventilation as used here to a scripted procedure of shallower, more frequent ventilation as will be used during the fMRI acquisition. We will also conduct more tests of labeling duration and post-labeling delay. Older or larger sea lions may benefit from a longer PLD if they have greater arterial transit times. However, healthy older sea lions are also expected to have higher hematocrit, hence a shorter blood T<sub>1</sub>, which could result in low SNR of labeled images when using longer PLD. Furthermore, the assumed brain/blood partition coefficient and blood T<sub>1</sub> estimates derive from human work that may not be appropriate for sea lions. The range of hematocrit values we observed across seven animals was large (0.28–0.47, median 0.40; see Table 1), in part due to age (7 months to 3 years) and overall health, but also perhaps because of differing splenic responses to anesthesia. In future, a multiple PLD approach may prove necessary for studying developing sea lions because the ATT may change with the animal's size, while the CBF itself may change with age. Sea lions in the range 6 months to 4 years correspond approximately to children from 2 to 16 years old. The CBF has been observed to be high in human infants, around 100 mL/100 g/min, dropping to ~80 mL/100 g/min by 8–9 years old (Suzuki, 1990; Satterthwaite et al., 2014). By age 18 the global CBF drops further, to a typical adult value of ~60 mL/100 g/min. In adulthood, there is a steady decrease to around 40 mL/100 g/min by age 70 (Dolui et al., 2016, 2017). Whether the sea lion brain follows a similar trajectory is an area for future research.

Manual ventilation appears to have caused a large artifact in our dMRI paradigm. Most likely the problem is due to chest motion - the through-space modulation of the magnetic field over the brain via chest magnetic susceptibility, and possibly some direct motion coupled to the head - rather than non-stationary blood gases as in the fMRI experiment. Presently, we acquire one non-DW image for every ten DW images, to be used as templates for eddy current and distortion corrections. In future, motion sensitivity can be reduced by ventilating during the non-DW images only, adding additional non-DW images to accommodate the ventilation if necessary, or perhaps with a reduced volume, higher rate ventilation procedure.

#### 4.1. Future directions

Improving the protocol beyond the present version would be feasible with a more sensitive receiver coil than the four-channel human neck

coil. A ring or a helmet coil with eight or more channels would permit the use of GRAPPA acceleration in 3D anatomical scanning, perhaps allowing higher spatial resolution in an acceptable scan time, and would also permit the use of SMS acquisitions for both the fMRI and dMRI scans. It is feasible to use low SMS factors with the human neck coil, but our pilot tests indicated some artifacts which were not worth the modest speed gains. A custom coil, designed with the constraints of anesthesia and animal monitoring in mind, would be preferable.

We have not yet had the opportunity to test a T<sub>2</sub>\*-weighted anatomical scan for susceptibility-weighted imaging (SWI) or quantitative susceptibility mapping (QSM). This sort of contrast is primarily used to detect hemorrhage but may also be useful for differentiating calcification, iron deposits and microbleeds (Liu et al., 2017). We would deploy the sequence in the event we observed pathology on one of the conventional anatomical scans. A future protocol might also include MP2RAGE for tissue and CSF segmentation (Wang et al., 2018), for enhanced deep GM contrast (Tanner et al., 2012; Okubo et al., 2016), or for detecting focal epileptogenic lesions (Kotikalapudi et al., 2019). The MP2RAGE could be a replacement for the MPRAGE we employed here. We will continue to test additional sequences as opportunities arise.

## 5. Conclusions

The protocol presented here establishes a broad framework for studying the neurological effects of exposure to the algal toxin domoic acid in developing sea lions. We propose that this protocol may also be a good starting point for MRI brain scanning of other marine mammals, including phocid seals, sea otters and perhaps even small cetaceans (dolphins and porpoises). While there is a large range of head and brain sizes and brain anatomies across marine mammals that might fit inside an MRI scanner, the tissue contrast is reasonably consistent across mammalian brains. We found respiration to be the greatest impediment to scan quality, and each scan type required careful tuning to overcome the largest artifacts. A different ventilation scheme or changes to the acquisition protocol are needed to fully mitigate the remaining consequences of manual ventilation in the fMRI and dMRI scans, and more experience is needed with CBF mapping to be able to interpret these results. Overall, however, the protocol is sufficient for routine use in developing sea lions.

### CRedit authorship contribution statement

**Peter F. Cook:** Conceptualization, Methodology, Formal analysis, Writing - original draft. **Vanessa A. Hoard:** Conceptualization, Methodology, Investigation, Writing - review & editing, Project administration. **Sudipto Dolui:** Methodology, Formal analysis, Writing - original draft. **Blaise deB Frederick:** Methodology, Formal analysis. **Richard Redfern:** Investigation, Resources. **Sophie E. Dennison:** Formal analysis, Writing - review & editing. **Barbie Halaska:** Resources. **Josh Bloom:** Methodology. **Kris T. Kruse-Elliott:** Methodology. **Emily R. Whitmer:** Investigation. **Emily J. Trumbull:** Investigation. **Gregory S. Berns:** Methodology. **John A. Detre:** Methodology, Resources. **Mark D'Esposito:** Resources, Funding acquisition. **Frances M.D. Gulland:** Conceptualization, Writing - review & editing. **Colleen Reichmuth:** Conceptualization, Writing - review & editing. **Shawn P. Johnson:** Resources, Supervision. **Cara L. Field:** Resources, Supervision, Project administration. **Ben A. Inglis:** Methodology, Investigation, Writing - original draft, Supervision, Project administration.

### Declaration of Competing Interest

The authors report no declarations of interest.

### Acknowledgements

We are indebted to the staff of The Marine Mammal Center, UC



Berkeley veterinarians Greg Lawson and Christie Ferrecchia, and the staff of Six Flags Discovery Kingdom for their animal welfare expertise. We thank the Wheeler Family Foundation for their generous support of the Henry H. Wheeler, Jr. Brain Imaging Center, and the National Science Foundation for support through their Major Research Instrumentation Program, award number BCS-0821855.

## References

- Alsop, D.C., Detre, J.A., Golay, X., Günther, M., Hendrikse, J., Hernandez-Garcia, L., Lu, H., MacIntosh, B.J., Parkes, L.M., Smits, M., van Osch, M.J., Wang, D.J., Wong, E.C., Zaharchuk, G., 2015. Recommended implementation of arterial spin-labeled perfusion MRI for clinical applications: a consensus of the ISMRM perfusion study group and the European consortium for ASL in dementia. *Magn. Reson. Med.* 73 (January 1), 102–116. <https://doi.org/10.1002/mrm.25197>.
- Arkipov, V., Kuleskaja, N., Lebedev, D., 2008. Behavioral perseveration and impairment of long-term memory in rats after intrahippocampal injection of kainic acid in subconvulsive dose. *Pharmacol. Biochem. Behav.* 88 (3), 299–305. <https://doi.org/10.1016/j.pbb.2007.08.012>.
- Aso, T., Urayama, S., Fukuyama, H., Murai, T., 2019. Axial variation of deoxyhemoglobin density as a source of the low-frequency time lag structure in blood oxygenation level-dependent signals. *PLoS One* 14 (9), e0222787. <https://doi.org/10.1371/journal.pone.0222787>.
- Barron, D.S., Tandon, N., Lancaster, J.L., Fox, P.T., 2014. Thalamic structural connectivity in medial temporal lobe epilepsy. *Epilepsia* 55 (6), e50–e55. <https://doi.org/10.1111/epi.12637>.
- Basser, P.J., Mattiello, J., LeBihan, D., 1994. Estimation of the effective self-diffusion tensor from the NMR spin echo. *J. Magn. Reson. B* 103 (3), 247–254. <https://doi.org/10.1006/jmrb.1994.1037>.
- Bates, S.S., Hubbard, K.A., Lundholm, N., Montresor, M., Leaw, C.P., 2018. Pseudo-nitzschia, Nitzschia, and domoic acid: new research since 2011. *Harmful Algae* 79, 3–43. <https://doi.org/10.1016/j.hal.2018.06.001>.
- Beckmann, C.F., Smith, S.M., 2004. Probabilistic independent component analysis for functional magnetic resonance imaging. *IEEE Trans. Med. Imaging* 23 (2), 137–152. <https://doi.org/10.1109/TMI.2003.822821>.
- Behrens, T.E., Woolrich, M.W., Jenkinson, M., Johansen-Berg, H., Nunes, R.G., Clare, S., Matthews, P.M., Brady, J.M., Smith, S.M., 2003. Characterization and propagation of uncertainty in diffusion-weighted MR imaging. *Magn. Reson. Med.* 50 (5), 1077–1088. <https://doi.org/10.1002/mrm.10609>.
- Behrens, T.E., Berg, H.J., Jbabdi, S., Rushworth, M.F., Woolrich, M.W., 2007. Probabilistic diffusion tractography with multiple fibre orientations: What can we gain? *Neuroimage* 34 (1), 144–155. <https://doi.org/10.1016/j.neuroimage.2006.09.018>.
- Behzadi, Y., Restom, K., Liu, J., Liu, T.T., 2007. A component based noise correction method (CompCor) for BOLD and perfusion based fMRI. *Neuroimage* 37 (1), 90–101.
- Bejarano, A.C., VanDolah, F.M., Gulland, F.M., Rowles, T.K., Schwacke, L.H., 2008. Production and toxicity of the marine biotoxin domoic acid and its effects on wildlife: a review. *Hum. Ecol. Risk Assess.* 14, 544–567.
- Berl, M.M., Walker, L., Modi, P., Irfanoglu, M.O., Sarlls, J.E., Nayak, A., Pierpaoli, C., 2015. Investigation of vibration-induced artifact in clinical diffusion-weighted imaging of pediatric subjects. *Hum. Brain Mapp.* 36 (12), 4745–4757. <https://doi.org/10.1002/hbm.22846>.
- Berns, G.S., Brooks, A.M., Spivak, M., Levy, K., 2017. Functional MRI in awake dogs predicts suitability for assistance work. *Sci. Rep.* 7, 43704. <https://doi.org/10.1038/srep43704>.
- Birn, R.M., Molloy, E.K., Patriat, R., Parker, T., Meier, T.B., Kirk, G.R., Nair, V.A., Meyerand, M.E., Prabhakaran, V., 2013. The effect of scan length on the reliability of resting-state fMRI connectivity estimates. *Neuroimage* 83, 550–558. <https://doi.org/10.1016/j.neuroimage.2013.05.099>.
- Brodie, E.C., Gulland, F.M.D., Greig, D.J., Hunter, M., Jaakola, J., St Leger, J., Leighfield, T.A., Van Dolah, F.M., 2006. Domoic acid causes reproductive failure in California sea lions (*Zalophus californianus*). *Mar. Mammal Sci.* 22 (3), 700–707. <https://doi.org/10.1111/j.1748-7692.2006.00045.x>.
- Buckmaster, P.S., Wen, X., Toyoda, I., Gulland, F.M., Van Bonn, W., 2014. Hippocampal neuropathology of domoic acid-induced epilepsy in California sea lions (*Zalophus californianus*). *J. Comp. Neurol.* 522 (7), 1691–1706. <https://doi.org/10.1002/cne.23509>.
- Concha, L., Livy, D.J., Beaulieu, C., Wheatley, B.M., Gross, D.W., 2010. In vivo diffusion tensor imaging and histopathology of the fimbria-fornix in temporal lobe epilepsy. *J. Neurosci.* 30 (3), 996–1002. <https://doi.org/10.1523/JNEUROSCI.1619-09.2010>.
- Cook, P., Reichmuth, C., Gulland, F., 2011. Rapid behavioural diagnosis of domoic acid toxicosis in California sea lions. *Biol. Lett.* 7 (4), 536–538. <https://doi.org/10.1098/rsbl.2011.0127>.
- Cook, P.F., Reichmuth, C., Rouse, A.A., Libby, L.A., Dennison, S.E., Carmichael, O.T., Kruse-Elliott, K.T., Bloom, J., Singh, B., Fravel, V.A., Barbosa, L., Stuppino, J.J., Van Bonn, W.G., Gulland, F.M., Ranganath, C., 2015. Algal toxin impairs sea lion memory and hippocampal connectivity, with implications for strandings. *Science* 350 (6267), 1545–1547. <https://doi.org/10.1126/science.aac5675>.
- Cook, P.F., Reichmuth, C., Rouse, A., Dennison, S., Van Bonn, B., Gulland, F., 2016. Natural exposure to domoic acid causes behavioral perseveration in wild sea lions: neural underpinnings and diagnostic application. *Neurotoxicol. Teratol.* 57, 95–105. <https://doi.org/10.1016/j.ntt.2016.08.001>.
- Cook, P.F., Berns, G.S., Colegrove, K., Johnson, S., Gulland, F., 2018. Postmortem DTI reveals altered hippocampal connectivity in wild sea lions diagnosed with chronic toxicosis from algal exposure. *J. Comp. Neurol.* 526 (2), 216–228. <https://doi.org/10.1002/cne.24317>.
- Costa, L.G., Giordano, G., Faustman, E.M., 2010. Domoic acid as a developmental neurotoxin. *Neurotoxicology* 31 (5), 409–423. <https://doi.org/10.1016/j.neuro.2010.05.003>.
- Detre, J.A., Alsop, D.C., 1999. Perfusion magnetic resonance imaging with continuous arterial spin labeling: methods and clinical applications in the central nervous system. *Eur. J. Radiol.* 30 (2), 115–124.
- Dinkelacker, V., Valabregue, R., Thivard, L., Lehericy, S., Baulac, M., Samson, S., Dupont, S., 2015. Hippocampal-thalamic wiring in medial temporal lobe epilepsy: enhanced connectivity per hippocampal voxel. *Epilepsia* 56 (8), 1217–1226. <https://doi.org/10.1111/epi.13051>.
- Dolui, S., Wang, Z., Wang, D.J.J., Mattay, R., Finkel, M., Elliott, M., Desiderio, L., Inglis, B., Mueller, B., Stafford, R.B., Launer, L.J., Jacobs Jr., D.R., Bryan, R.N., Detre, J.A., 2016. Comparison of non-invasive MRI measurements of cerebral blood flow in a large multisite cohort. *J. Cereb. Blood Flow Metab.* 36 (7), 1244–1256. <https://doi.org/10.1177/0271678X16646124>.
- Dolui, S., Vidorreta, M., Wang, Z., Nasrallah, I.M., Alavi, A., Wolk, D.A., Detre, J.A., 2017. Comparison of PASL, PCASL, and background-suppressed 3D PCASL in mild cognitive impairment. *Hum. Brain Mapp.* 38 (10), 5260–5273. <https://doi.org/10.1002/hbm.23732>.
- Dolui, S., Tisdall, D., Vidorreta, M., Jacobs Jr, D.R., Nasrallah, I.M., Bryan, R.N., Wolk, D.A., Detre, J.A., 2019. Characterizing a perfusion-based periventricular small vessel region of interest. *Neuroimage Clin.* 23, 101897. <https://doi.org/10.1016/j.nicl.2019.101897>.
- Eichenbaum, H., 2000. A cortical-hippocampal system for declarative memory. *Nat. Rev. Neurosci.* 1 (1), 41–50. <https://doi.org/10.1038/35036213>.
- Eichenbaum, H., Komorowski, R., MacDonald, C.J., Kraus, B.J., Robitsek, J., 2016. How does the hippocampus support the spatial and temporal attributes of memory? In: Jackson, P.A., Chiba, A.A., Berman, R.F., Ragozzino, M.E. (Eds.), *The Neurobiological Basis of Memory*. Springer International Publishing, pp. 39–57.
- Foxley, S., Jbabdi, S., Clare, S., Lam, W., Ansoorge, O., Douaud, G., Miller, K., 2014. Improving diffusion-weighted imaging of post-mortem human brains: SSFP at 7 T. *Neuroimage* 102 (Pt 2), 579–589. <https://doi.org/10.1016/j.neuroimage.2014.08.014>.
- Frederick, B., 2020. PICaChooSer [Computer Software]. <https://doi.org/10.5281/zenodo.3924099>. <https://github.com/bbfrederick/picachoser>.
- Gallichan, D., Scholz, J., Bartsch, A., Behrens, T.E., Robson, M.D., Miller, K.L., 2010. Addressing a systematic vibration artifact in diffusion-weighted MRI. *Hum. Brain Mapp.* 31 (2), 193–202. <https://doi.org/10.1002/hbm.20856>.
- Goldstein, T., Mazet, J.A., Zabka, T.S., Langlois, G., Colegrove, K.M., Silver, M., Bargu, S., Van Dolah, F., Leighfield, T., Conrad, P.A., Barakos, J., Williams, D.C., Dennison, S., Haulena, M., Gulland, F.M., 2008. Novel symptomatology and changing epidemiology of domoic acid toxicosis in California sea lions (*Zalophus californianus*): an increasing risk to marine mammal health. *Proc. Biol. Sci.* 275 (1632), 267–276. <https://doi.org/10.1098/rspb.2007.1221>.
- Griswold, M.A., Jakob, P.M., Heidemann, R.M., Nittka, M., Jellus, V., Wang, J., Kiefer, B., Haase, A., 2002. Generalized autocalibrating partially parallel acquisitions (GRAPPA). *Magn. Reson. Med.* 47 (6), 1202–1210.
- Gulland, F.M., Haulena, M., Fauquier, D., Langlois, G., Lander, M.E., Zabka, T., Duerr, R., 2002. Domoic acid toxicity in Californian sea lions (*Zalophus californianus*): clinical signs, treatment and survival. *Vet. Rec.* 150 (15), 475–480. <https://doi.org/10.1136/vr.150.15.475>.
- Guo, X., Xu, S., Wang, G., Zhang, Y., Guo, L., Zhao, B., 2015. Asymmetry of cerebral blood flow measured with three-dimensional pseudocontinuous arterial spin-labeling mr imaging in temporal lobe epilepsy with and without mesial temporal sclerosis. *J. Magn. Reson. Imaging* 42 (5), 1386–1397. <https://doi.org/10.1002/jmri.24920>.
- Jenkinson, M., Smith, S.M., 2001. A global optimisation method for robust affine registration of brain images. *Med. Image Anal.* 5 (2), 143–156.
- Jenkinson, M., Bannister, P.R., Brady, J.M., Smith, S.M., 2002. Improved optimisation for the robust and accurate linear registration and motion correction of brain images. *Neuroimage* 17 (2), 825–841.
- Kotikalapudi, R., Martin, P., Erb, M., Scheffler, K., Marquetand, J., Bender, B., Focke, N.K., 2019. MP2RAGE multispectral voxel-based morphometry in focal epilepsy. *Hum. Brain Mapp.* 40 (17), 5042–5055. <https://doi.org/10.1002/hbm.24756>.
- Kuroki, N., Kubicki, M., Nestor, P.G., Salisbury, D.F., Park, H.-J., Levitt, J.L., Woolston, S., Frumin, M., Niznikiewicz, M., Westin, C.-F., Maier, S.E., McCarley, R.W., Shenton, M.E., 2006. Fornix integrity and hippocampal volume in male schizophrenic patients. *Biol. Psychiatry* 60 (1), 22–31. <https://doi.org/10.1016/j.biopsych.2005.09.021>.
- Lavenex, P., Amaral, D.G., 2000. Hippocampal-neocortical interaction: a hierarchy of associativity. *Hippocampus* 10 (4), 420–430.
- Lefebvre, K.A., Frame, E.R., Kendrick, P.S., 2012. Domoic acid and fish behavior: a review. *Harmful Algae* 13, 126–130. <https://doi.org/10.1016/j.hal.2011.09.011>.
- Lefebvre, K.A., Hendrix, A., Halaska, B., Duijgnan, P., Shum, S., Isoherranen, N., Marcinek, D.J., Gulland, F.M.D., 2018. Domoic acid in California sea lion fetal fluids indicates continuous exposure to a neuroteratogen poses risks to mammals. *Harmful Algae* 79, 53–57. <https://doi.org/10.1016/j.hal.2018.06.003>.
- Li, W., Liu, P., Lu, H., Strouse, J.J., van Zijl, P.C.M., Qin, Q., 2017. Fast measurement of blood T1 in the human carotid artery at 3 T: accuracy, precision, and reproducibility. *Magn. Reson. Med.* 77 (6), 2296–2302. <https://doi.org/10.1002/mrm.26325>.
- Liu, T.T., 2016. Noise contributions to the fMRI signal: an overview. *Neuroimage* 143, 141–151. <https://doi.org/10.1016/j.neuroimage.2016.09.008>.

- Liu, S., Buch, S., Chen, Y., Choi, H.-S., Dai, Y., Habib, C., Hu, J., Jung, J.-Y., Luo, Y., Utraieni, D., Wang, M., Wu, D., Xia, S., Haacke, E.M., 2017. Susceptibility-weighted imaging: current status and future directions. *NMR Biomed.* 30 (4) <https://doi.org/10.1002/nbm.3552> doi:10.1002/nbm.3552.
- Mabray, P., Thewamit, R., Whitehead, M.T., Kao, A., Scafidì, J., Gaillard, W.D., Chang, T., Tsuchida, T.N., 2018. Increased cerebral blood flow on arterial spin labeling magnetic resonance imaging can localize to seizure focus in newborns: a report of 3 cases. *Epilepsia* 59 (5), e63–e67. <https://doi.org/10.1111/epi.14060>.
- McCabe, R.M., Hickey, B.M., Kudela, R.M., Lefebvre, K.A., Adams, N.G., Bill, B.D., Gulland, F.M.D., Thomson, R.E., Cochlan, W.P., Trainer, V.L., 2016. An unprecedented coastwide toxic algal bloom linked to anomalous ocean conditions. *Geophys. Res. Lett.* 43 (19), 10–366. <https://doi.org/10.1002/2016GL070023>.
- McKibben, S.M., Peterson, W., Wood, A.M., Trainer, V.L., Hunter, M., White, A.E., 2017. Climatic regulation of the neurotoxin domoic acid. *Proc Natl Acad Sci U S A* 114 (2), 239–244. <https://doi.org/10.1073/pnas.1606798114>.
- Miller, K.L., McNab, J.A., Jbabdi, S., Douaud, G., 2012. Diffusion tractography of post-mortem human brains: optimization and comparison of spin echo and steady-state free precession techniques. *Neuroimage* 59 (3), 2284–2297. <https://doi.org/10.1016/j.neuroimage.2011.09.054>.
- Montie, E.W., Pussini, N., Schneider, G.E., Battey, T.W., Dennison, S., Barakos, J., Gulland, F., 2009. Neuroanatomy and volumes of brain structures of a live California sea lion (*Zalophus californianus*) from magnetic resonance images. *Anat. Rec.* 292 (10), 1523–1547. <https://doi.org/10.1002/ar.20937>.
- Montie, E.W., Wheeler, E., Pussini, N., Battey, T.W., Barakos, J., Dennison, S., Colegrove, K., Gulland, F., 2010. Magnetic resonance imaging quality and volumes of brain structures from live and postmortem imaging of California sea lions with clinical signs of domoic acid toxicosis. *Dis Aquat Organ* 91 (3), 243–256. <https://doi.org/10.3354/dao02259>.
- Montie, E.W., Wheeler, E., Pussini, N., Battey, T.W., Van Bonn, W., Gulland, F., 2012. Magnetic resonance imaging reveals that brain atrophy is more severe in older California sea lions with domoic acid toxicosis. *Harmful Algae* 20, 19–29. <https://doi.org/10.1016/j.hal.2012.07.004>.
- Moser, M.B., Moser, E.I., 1998. Functional differentiation in the hippocampus. *Hippocampus* 8 (6), 608–619 doi: 10.1002/(SICI)1098-1063(1998)8:6<608::AID-HIPO3>3.0.CO;2-7.
- Mugler 3rd, J.P., 2014. Optimized three-dimensional fast-spin-echo MRI. *J. Magn. Reson. Imaging* 39 (4), 745–767. <https://doi.org/10.1002/jmri.24542>.
- Newberg, A.B., Wang, J., Rao, H., Swanson, R.L., Wintering, N., Karp, J.S., Alavi, A., Greenberg, J.H., Detre, J.A., 2005. Concurrent CBF and CMRGLC changes during human brain activation by combined fMRI-PET scanning. *Neuroimage* 28 (2), 500–506.
- Nguyen, D., Kapina, V., Seeck, M., Viallon, M., Fedespiel, A., Lovblad, K.O., 2010. Ictal hyperperfusion demonstrated by arterial spin-labeling MRI in status epilepticus. *J. Neuroradiol.* 37 (4), 250–251. <https://doi.org/10.1016/j.neurad.2009.12.003>.
- Okubo, G., Okada, T., Yamamoto, A., Kanagaki, M., Fushimi, Y., Okada, T., Murata, K., Togashi, K., 2016. MP2RAGE for deep gray matter measurement of the brain: a comparative study with MPRAE. *J. Magn. Reson. Imaging* 43 (1), 55–62. <https://doi.org/10.1002/jmri.24960>.
- Otte, W.M., van Eijsden, P., Sander, J.W., Duncan, J.S., Dijkhuizen, R.M., Braun, K.P., 2012. A meta-analysis of white matter changes in temporal lobe epilepsy as studied with diffusion tensor imaging. *Epilepsia* 53 (4), 659–667. <https://doi.org/10.1111/j.1528-1167.2012.03426.x>.
- Petroff, R., Richards, R., Crouthamer, B., McKain, N., Stanley, C., Grant, K.S., Shum, S., Jing, J., Isoherranen, N., Burbacher, T.M., 2019. Chronic, low-level oral exposure to marine toxin, domoic acid, alters whole brain morphometry in nonhuman primates. *Neurotoxicology* 72, 114–124. <https://doi.org/10.1016/j.neuro.2019.02.016>.
- Ramsdell, J.S., Gulland, F.M., 2014. Domoic acid epileptic disease. *Mar. Drugs* 12 (3), 1185–1207. <https://doi.org/10.3390/md12031185>.
- Ranganath, C., Heller, A., Cohen, M.X., Brozinsky, C.J., Rissman, J., 2005. Functional connectivity with the hippocampus during successful memory formation. *Hippocampus* 15 (8), 997–1005. <https://doi.org/10.1002/hipo.20141>.
- Rusbridge, C., Long, S., Jovanovic, J., Milne, M., Berendt, M., Bhatti, S.F., De Risio, L., Farquhar, R.G., Fischer, A., Matissek, K., Muñana, K., Patterson, E.E., Pakozdy, A., Penderis, J., Platt, S., Podell, M., Potschka, H., Stein, V.M., Tipold, A., Volk, H.A., 2015. International Veterinary Epilepsy Task Force recommendations for a veterinary epilepsy-specific MRI protocol. *BMC Vet. Res.* 11, 194. <https://doi.org/10.1186/s12917-015-0466-x>.
- Rust, L., Gulland, F., Frame, E., Lefebvre, K., 2014. Domoic acid in milk of free living California marine mammals indicates lactational exposure occurs. *Mar Mam Sci.* 30 (3), 1272–1278. <https://doi.org/10.1111/mms.12117>.
- Satterthwaite, T.D., Shinohara, R.T., Wolf, D.H., Hopson, R.D., Elliott, M.A., Vandekar, S. N., Ruparel, K., Calkins, M.E., Roalf, D.R., Gennatas, E.D., Jackson, C., Erus, G., Prabhakaran, K., Davatzikos, C., Detre, J.A., Hakonarson, H., Gur, R.C., Gur, R.C.E., 2014. Impact of puberty on the evolution of cerebral perfusion during adolescence. *Proc Natl Acad Sci U S A* 111 (23), 8643–8648. <https://doi.org/10.1073/pnas.1400178111>.
- Scholín, C.A., Gulland, F., Doucette, G.J., Benson, S., Busman, M., Chavez, F.P., Cordaro, J., DeLong, R., De Vogelaere, A., Harvey, J., Haulena, M., Lefebvre, K., Lipscomb, T., Loscutoff, S., Lowenstine, L.J., Marin 3rd, R., Miller, P.E., McLellan, W. A., Moeller, P.D., Powell, C.L., Rowles, T., Silvagni, P., Silver, M., Spraker, T., Trainer, V., Van Dolah, F.M., 2000. Mortality of sea lions along the central California coast linked to a toxic diatom bloom. *Nature* 403 (6765), 80–84.
- Silvagni, P.A., Lowenstine, L.J., Spraker, T., Lipscomb, T.P., Gulland, F.M., 2005. Pathology of domoic acid toxicity in California sea lions (*Zalophus californianus*). *Vet. Pathol.* 42 (2), 184–191. <https://doi.org/10.1354/vp.42-2-184>.
- Stein, T., Moritz, C., Quigley, M., Cordes, D., Haughton, V., Meyerand, E., 2000. Functional connectivity in the thalamus and hippocampus studied with functional MR imaging. *AJNR Am. J. Neuroradiol.* 21 (8), 1397–1401.
- Suzuki, K., 1990. The changes of regional cerebral blood flow with advancing age in children. *Nagoya Med. J.* 34, 159–170.
- Tanner, M., Gamberato, G., Kober, T., Krueger, G., Erritzoe, D., Marques, J.P., Newbould, R., 2012. Fluid and white matter suppression with the MP2RAGE sequence. *J. Magn. Reson. Imaging* 35 (5), 1063–1070. <https://doi.org/10.1002/jmri.23532>.
- Thomas, K., Harvey, J.T., Goldstein, T., Barakos, J., Gulland, F., 2010. Movement, dive behavior, and survival of California sea lions (*Zalophus californianus*) posttreatment for domoic acid toxicosis. *Marine Mamm Sci* 26, 36–52.
- Tong, Y., Frederick, B.D., 2010. Time lag dependent multimodal processing of concurrent fMRI and near-infrared spectroscopy (NIRS) data suggests a global circulatory origin for low-frequency oscillation signals in human brain. *Neuroimage* 53 (2), 553–564. <https://doi.org/10.1016/j.neuroimage.2010.06.049>.
- Tong, Y., Frederick, B.D., 2014. Tracking cerebral blood flow in BOLD fMRI using recursively generated regressors. *Hum. Brain Mapp.* 35 (11), 5471–5485. <https://doi.org/10.1002/hbm.22564>.
- Tong, Y., Hocke, L.M., Nickerson, L.D., Licata, S.C., Lindsey, K.P., Bd, Frederick, 2013. Evaluating the effects of systemic low frequency oscillations measured in the periphery on the independent component analysis results of resting state networks. *Neuroimage* 76, 202–215. <https://doi.org/10.1016/j.neuroimage.2013.03.019>.
- Tong, Y., Hocke, L.M., Frederick, B.B., 2019. Low frequency systemic hemodynamic “Noise” in resting state BOLD fMRI: characteristics, causes, implications, mitigation strategies, and applications. *Front. Neurosci.* 13, 787. <https://doi.org/10.3389/fnins.2019.00787>.
- Van Bonn, W., Montie, E., Dennison, S., Pussini, N., Cook, P., Greig, D., Barakos, J., Colegrove, K., Gulland, F., 2011. Evidence of injury caused by gas bubbles in a live marine mammal: barotrauma in a California sea lion *Zalophus californianus*. *Dis Aquat Organ.* 96 (2), 89–96. <https://doi.org/10.3354/dao02376>.
- Van Bonn, W., Dennison, S., Cook, P., Fahlman, A., 2013. Gas bubble disease in the brain of a living California sea lion (*Zalophus californianus*). *Front. Physiol.* 4, 5. <https://doi.org/10.3389/fphys.2013.00005>.
- Van de Moortele, P.F., Pfeuffer, J., Glover, G.H., Ugurbil, K., Hu, X., 2002. Respiration-induced B0 fluctuations and their spatial distribution in the human brain at 7 Tesla. *Magn. Reson. Med.* 47 (5), 888–895.
- Vidorreta, M., Baiteau, E., Wang, Z., De Vita, E., Pastor, M.A., Thomas, D.L., Detre, J.A., Fernández-Seara, M.A., 2014. Evaluation of segmented 3D acquisition schemes for whole-brain high-resolution arterial spin labeling at 3 T. *NMR Biomed.* 27 (11), 1387–1396. <https://doi.org/10.1002/nbm.3201>.
- Vidorreta, M., Wang, Z., Chang, Y.V., Wolk, D.A., Fernández-Seara, M.A., Detre, J.A., 2017. Whole-brain background-suppressed pCASL MRI with 1D-accelerated 3D RARE Stack-Of-Spirals readout. *PLoS One* 12 (8), e0183762. <https://doi.org/10.1371/journal.pone.0183762>.
- Wald, L.L., Polimeni, J.R., 2017. Impacting the effect of fMRI noise through hardware and acquisition choices - Implications for controlling false positive rates. *Neuroimage* 154, 15–22. <https://doi.org/10.1016/j.neuroimage.2016.12.057>.
- Wang, Y., Wang, Y., Zhang, Z., Xiong, Y., Zhang, Q., Yuan, C., Guo, H., 2018. Segmentation of gray matter, white matter, and CSF with fluid and white matter suppression using MP2RAGE. *J. Magn. Reson. Imaging* 48 (6), 1540–1550. <https://doi.org/10.1002/jmri.26014>.
- Weiner, M.W., Veitch, D.P., Aisen, P.S., Beckett, L.A., Cairns, N.J., Green, R.C., Harvey, D., Jack Jr., C.R., Jagust, W., Morris, J.C., Petersen, R.C., Salazar, J., Saykin, A.J., Shaw, L.M., Toga, A.W., Trojanowski, J.Q., 2017. Alzheimer’s disease neuroimaging initiative. The alzheimer’s disease neuroimaging initiative 3: continued innovation for clinical trial improvement. *Alzheimers Dement.* 13 (5), 561–571. <https://doi.org/10.1016/j.jalz.2016.10.006>.
- Wellmer, J., Quesada, C.M., Rothe, L., Elger, C.E., Bien, C.G., Urbach, H., 2013. Proposal for a magnetic resonance imaging protocol for the detection of epileptogenic lesions at early outpatient stages. *Epilepsia* 54 (11), 1977–1987. <https://doi.org/10.1111/epi.12375>.
- Wise, R.G., Ide, K., Poulin, M.J., Tracey, I., 2004. Resting fluctuations in arterial carbon dioxide induce significant low frequency variations in BOLD signal. *Neuroimage* 21 (4), 1652–1664. <https://doi.org/10.1016/j.neuroimage.2003.11.025>.
- Wohlrab, S., John, U., Klemm, K., Eberlein, T., Forsberg Grivogiannis, A.M., Krock, B., Frickenhaus, S., Bach, L.T., Rost, B., Riebesell, U., Van de Waal, D.B., 2020. Ocean acidification increases domoic acid contents during a spring to summer succession of coastal phytoplankton. *Harmful Algae* 92, 101697. <https://doi.org/10.1016/j.hal.2019.101697>.
- Wolf, R.L., Alsop, D.C., Levy-Reis, I., Meyer, P.T., Maldjian, J.A., Gonzalez-Atavales, J., French, J.A., Alavi, A., Detre, J.A., 2001. Detection of mesial temporal lobe hypoperfusion in patients with temporal lobe epilepsy by use of arterial spin labeled perfusion MR imaging. *AJNR Am. J. Neuroradiol.* 22 (7), 1334–1341.
- Woolrich, M.W., Ripley, B.D., Brady, M., Smith, S.M., 2001. Temporal autocorrelation in univariate linear modeling of FMRI data. *NeuroImage* 14 (6), 1370–1386. <https://doi.org/10.1006/nimg.2001.0931>.
- Wu, Y.C., Alexander, A.L., 2007. Hybrid diffusion imaging. *Neuroimage* 36 (3), 617–629.
- Wu, W.C., Fernández-Seara, M., Detre, J.A., Wehrli, F.W., Wang, J., 2007. A theoretical and experimental investigation of the tagging efficiency of pseudocontinuous arterial spin labeling. *Magn. Reson. Med.* 58 (5), 1020–1027.
- Yeh, F.-C., Verstynen, T.D., Wang, Y., Fernández-Miranda, J.C., Tseng, W.-Y.I., 2013. Deterministic diffusion Fiber tracking improved by quantitative anisotropy. *PLoS One* 8 (11), e80713. <https://doi.org/10.1371/journal.pone.0080713>.
- Yoo, R.E., Yun, T.J., Yoon, B.W., Lee, S.K., Lee, S.K.T., Kang, K.M., Choi, S.H., Kim, J.H., Sohn, C.H., Park, S.W., Han, M.H., 2017. Identification of cerebral perfusion using

- arterial spin labeling in patients with seizures in acute settings. *PLoS One* 12 (3), e0173538. <https://doi.org/10.1371/journal.pone.0173538>.
- Zhang, Y., Brady, M., Smith, S., 2001. Segmentation of brain MR images through a hidden Markov random field model and the expectation-maximization algorithm. *IEEE Trans Med Imag.* 20 (1), 45–57.
- Zhao, L., Vidorreta, M., Soman, S., Detre, J.A., Alsop, D.C., 2017. Improving the robustness of pseudo-continuous arterial spin labeling to off-resonance and pulsatile flow velocity. *Magn. Reson. Med.* 78 (4), 1342–1351. <https://doi.org/10.1002/mrm.26513>.
- Zhu, Z., Qu, P., Fu, F., Tennenbaum, N., Tatters, A.O., Hutchins, D.A., 2017. Understanding the blob bloom: warming increases toxicity and abundance of the harmful bloom diatom *Pseudo-nitzschia* in California coastal waters. *Harmful Algae* 67, 36–43. <https://doi.org/10.1016/j.hal.2017.06.004>.
- Zuloaga, D.G., Lahvis, G.P., Mills, B., Pearce, H.L., Turner, J., Raber, J., 2016. Fetal domoic acid exposure affects lateral amygdala neurons, diminishes social investigation and alters sensory-motor gating. *Neurotoxicology* 53, 132–140. <https://doi.org/10.1016/j.neuro.2016.01.007>.